TriDurLE

National Center for Transportation Infrastructure Durability & Life-Extension

Project ID: 2021-WSU-01

Design of Fly Ash-Based Geopolymer Concrete-Filled CFRP Tube Composite For Highly Durable and Environmentally Friendly Infrastructure

Final Report

By

PI: Xianming Shi, PhD, F. ASCE, Professor, Washington State University
Co-PI: Zhipeng Li, Postdoc Research Associate, Washington State University

for

National University Transportation Center TriDurLE
Department of Civil & Environmental Engineering
405 Spokane Street PO Box 642910
Washington State University Pullman, WA 99164-2910

Date
03/31/2025

Acknowledgements

The work presented in this report was sponsored by the National Center for Transportation Infrastructure Durability & Life Extension (TriDurLE) and 2020 David C. Gross Scholarship from the American Coal Ash Association Educational Foundation (ACAAEF), and this support is gratefully acknowledged. The authors also wish to express their sincere appreciation to the individuals who contributed to this work. Mr. Jan Benedict B. Mislang, who served as an undergraduate research assistant and is now a transportation engineer at the Washington State Department of Transportation, provided technical support during the research. The authors also thank Dr. Zhen Lei, Associate Professor at Yunnan University, China, and visiting scholar at Washington State University, for his insightful discussions and intellectual contributions.

Disclaimer

Table of Contents

List of Figures

List of Tables

Executive Summary

This report presents a three-stage research endeavor focused on developing and evaluating a novel graphene oxide (GO)-modified, class C fly ash-based geopolymer binder as a sustainable alternative to ordinary portland cement (OPC) for structural applications. The overarching goal is to enhance the mechanical performance, durability, and environmental sustainability of geopolymer composites through nanotechnology and advanced material design.

In the first phase, a clinker-free cementitious binder primarily composed of Class C fly ash was engineered using a systematic uniform design experimental approach. Incorporation of a trace amount of graphene oxide (GO, 0.02 wt.%) produced a GO-engineered alkali-activated fly ash-based geopolymer (GFAGPR) paste, resulting in 6.1% and 9.3% increases in 7-day and 28-day compressive strength, respectively, acceleration of setting time from 8 min to 7 min, a 43% reduction in water absorption, and an 88% increase in water contact angle (from 16° to 30°). Microstructural analyses (SEM, XRD, TGA, and EDS) confirmed that GO promoted the formation and more uniform distribution of hydration gels, primarily C-(A)-S-H, by acting as a micro-/nanoscale template within the geopolymer matrix.

In the second phase, freeze–thaw (F/T) durability of the geopolymer binder was evaluated under rapid cycling in accordance with ASTM C666. The GO-modified geopolymer exhibited substantially improved durability; after approximately 48 F/T cycles, the GFAGPR paste experienced only about a 6% reduction in compressive strength, whereas the compressive strength of the unmodified FAGPR paste decreased by approximately 33%. Spectroscopic analyses indicated that GO incorporation reduced calcium leaching, refined pore structure, and enhanced gel stability, thereby mitigating microcrack development and strength degradation under cold-climate exposure conditions.

In the final phase, the GFAGPR binder was used to fabricate concrete-filled carbon fiber-reinforced polymer (CFRP) tube composites, aimed at achieving both mechanical enhancement and environmental benefits. Axial compression tests showed substantial improvements in confined compressive strength, with the GFAGPR composite outperforming both OPC- and FAGPR counterparts. A cradle-to-grave life cycle assessment (LCA) conducted over a 100-year service life indicated that GFAGPR-filled CFRP tube systems can reduce global warming potential (GWP) by more than 30% compared to conventional OPC-based CFRP composites while maintaining equivalent or superior structural performance. Although CFRP materials introduce higher initial material costs, the enhanced compressive strength of the geopolymer core enables reduced CFRP usage and extended service life, resulting in a balanced sustainability–cost–performance profile for long-term infrastructure applications.

In conclusion, this study establishes a technically feasible and environmentally superior pathway for developing high-performance, GO-modified geopolymer-based infrastructure materials. The results offer promising implications for sustainable construction, particularly in cold regions or applications demanding high durability and resilience.

Chapter 1. Introduction

1.1 Problem Statement

The cement and concrete industry, while foundational to global infrastructure, is a major contributor to anthropogenic CO_2 emissions, primarily due to the energy-intensive production of ordinary portland cement (OPC), which alone accounts for approximately 8–9% of global CO_2 output. In response to increasingly stringent sustainability goals and carbon neutrality targets, there is a growing demand for low-carbon, high-performance cementitious materials that can reduce the reliance on OPC while maintaining or exceeding the required mechanical and durability performance for structural applications.

Alkali-activated materials (AAMs), particularly those based on class C fly ash, an abundant industrial byproduct, have demonstrated significant promise as clinker-free alternatives to OPC. These materials offer a potential reduction in embodied carbon and energy demand, aligning well with circular economic principles. However, their broader deployment in structural concrete has been hampered by three critical challenges: Inconsistent and often substandard early-age mechanical performance, including setting characteristics and strength development, which can vary significantly due to the heterogeneous nature of source materials and the complexity of activation chemistry; Limited durability, especially in cold climates where cyclic thermal stresses and moisture intrusion lead to microcracking, scaling, and long-term degradation. Current fly ash-based geopolymers remain vulnerable under such environmental stressors, limiting their field applicability; and Structural-level limitations, where the compressive strength and ductility of geopolymer concrete may not meet code requirements for load-bearing elements, especially in unconfined configurations. Without structural enhancement, these materials remain underutilized in primary infrastructure systems.

To address these bottlenecks, graphene oxide (GO) has emerged as a multifunctional nanomaterial capable of enhancing the performance of geopolymer binders through multiple synergistic mechanisms, including refinement of pore structure, promotion of gel polymerization (C-S-H/C-A-S-H), and improvement of mechanical strength and durability via nano-filler and charge-balancing effects. However, existing studies are fragmented and often lack systematic evaluation across both material and durability dimensions. Furthermore, fiber-reinforced polymer (FRP) tube confinement, particularly when using lightweight and corrosion-resistant carbon fiber-reinforced polymer (CFRP), offers an efficient approach to boost the load-carrying capacity and ductility of concrete elements. However, the integration of GO-enhanced geopolymer concrete with CFRP tube confinement has not been thoroughly explored, especially with respect to its long-term sustainability performance.

This research directly addresses the above challenges by developing and validating a GO-modified, alkali-activated fly ash binder system, assessing its freeze-thaw durability and microstructural evolution, and finally applying it in CFRP-tube confined composite columns. A cradle-to-grave life cycle assessment (LCA) is conducted to quantify both the

environmental impacts and economic feasibility of these advanced materials compared to traditional OPC-based systems. The outcome is a multiscale, technically validated, and sustainability-oriented material solution with clear implications for resilient and low-carbon infrastructure in both civil and industrial construction.

1.2 Objectives

This research aims to develop a GO-engineered, alkali-activated fly ash-based geopolymer binder system, and apply it within CFRP tube-confined structural composites, to comprehensively enhance their mechanical performance and environmental sustainability. The specific objectives are as follows:

(1) Material Development and Optimization: Formulate a clinker-free and chloride-free GO-engineered FAGPR, optimized through a statistical design of experiments to achieve desirable early-age strength, dimensional stability, and workability; and investigate the influence of GO on hydration kinetics, gel morphology, pore structure, and interfacial properties, and establish a microstructure–property relationship model to guide material design.

(2) Durability Enhancement and Mechanistic Understanding: Evaluate the freeze–thaw resistance of the GO-modified geopolymer paste (GFAGPR), focusing on strength retention, moisture migration, and carbonation behavior under cyclic freezing conditions; and apply advanced multiscale characterization techniques (XRD, SEM, EDS, FTIR, NMR, TGA) to elucidate the mechanisms by which GO regulates Ca^{2+} migration, enhances gel polymerization, and contributes to microstructural densification.

(3) Structural Enhancement and Modeling: Fabricate and test CFRP tube-confined geopolymer concrete composites using both unmodified and GO-modified binders, and assess their axial load capacity, deformation behavior, and failure modes; and develop and validate mechanical response and confinement models suitable for predicting the behavior of these advanced hybrid composites under compressive loading, with a view toward practical structural applications.

(4) Life Cycle Assessment and Engineering Feasibility: Establish a cradle-to-grave life cycle assessment (LCA) model encompassing material production, construction, service life, and end-of-life phases, to quantify carbon footprint (GWP) and life-cycle cost; and Benchmark the GO-enhanced CFRP composite columns against OPC-based systems, identifying performance–sustainability–cost tradeoffs and verifying the technical and economic viability of the proposed system for large-scale deployment.

By achieving these objectives, this research will contribute to the development of a low-carbon, high-performance, and resilient construction material system, with significant implications for sustainable infrastructure and material innovation in both civil engineering and industrial sectors.

1.3 Expected Contributions

This research is expected to make the following key contributions to the fields of sustainable construction materials, nanomodified geopolymers, and advanced structural

composites:

(1) Development of a Novel GO-Engineered, Clinker-Free Binder System: Deliver a scientifically validated, graphene oxide-modified alkali-activated fly ash binder (PAFA) that is entirely free of Portland cement and chlorides, with improved mechanical properties, rapid setting, and minimal volumetric instability; and provide an optimized material formulation supported by microstructural and chemical evidence, laying the groundwork for next-generation low-carbon cementitious systems.

(2) Mechanistic Understanding of GO's Role in Enhancing Durability: Uncover the fundamental mechanisms by which GO improves freeze–thaw resistance and gel polymerization in geopolymer matrices through advanced characterization (XRD, SEM, EDS, FTIR, NMR, TGA); and demonstrate how GO enables improved Ca^{2+} retention, reduced moisture migration, and nanostructural refinement under aggressive environmental conditions.

(3) Structural Integration with CFRP for Enhanced Mechanical Performance: Introduce a novel hybrid material system by integrating GO-modified geopolymer concrete into CFRP tube confinement, achieving superior axial load capacity, post-peak ductility, and energy absorption; and establish predictive mechanical and confinement models applicable to structural design, offering a transferable framework for broader adoption of geopolymer-based FRP-confined composites.

(4) Comprehensive Life Cycle Assessment and Sustainability Profiling: Quantitatively compare the environmental (GWP) and economic impacts of OPC, FAGPR, and GFAGPR-based CFRP composites over a 100-year service life using a cradle-to-grave LCA approach; and provide critical insight into how nano-enhancement and structural confinement can jointly reduce CFRP material demand, thereby mitigating both cost and carbon penalties.

(5) Bridging the Gap Between Materials Innovation and Structural Application: Offer a complete research-to-application pathway that spans from nano-level material design to structural-level implementation, demonstrating how nanotechnology and geopolymer chemistry can be synergistically combined to produce resilient, low-carbon structural systems; and contribute to the practical adoption of sustainable concrete technologies in cold regions and other demanding environments, supporting global decarbonization efforts in the construction sector.

1.4 Report Overview

This report is structured into five chapters that reflect a logical progression from problem identification to material development, experimental validation, and sustainability assessment.

Chapter 1 introduces the motivation and background of the study, addressing the urgent need for low-carbon, high-performance alternatives to ordinary Portland cement. It outlines the specific problem of limited strength and durability in conventional fly ash-based

geopolymer systems and proposes the integration of graphene oxide (GO) and CFRP tube confinement as a multiscale solution. This chapter also defines the research objectives, expected contributions, and provides an overview of the report structure.

Chapter 2 reviews the relevant literature on alkali-activated materials, nanomaterial-enhanced binders, freeze–thaw durability in geopolymer systems, and the mechanical behavior of FRP-confined concrete. It highlights the current limitations in the field, including incomplete understanding of GO's functional mechanisms, limited integration of structural confinement, and the lack of life-cycle-based performance comparisons, thereby establishing the research gap addressed in this study.

Chapter 3 details the methodology used to design, fabricate, and evaluate the proposed material systems. It includes the formulation of GO-modified geopolymer binders, the testing of their mechanical and durability performance, the preparation and axial testing of CFRP-confined specimens, and the implementation of a cradle-to-grave life cycle assessment (LCA) model. A suite of advanced analytical techniques (e.g., SEM, XRD, TGA, FTIR, NMR) is employed to investigate the material's microstructural and chemical behavior.

Chapter 4 presents and interprets the experimental results. The GO-modified binder exhibits improved strength, rapid setting, reduced shrinkage, and superior freeze–thaw resistance. Microstructural analyses reveal that GO enhances gel polymerization, stabilizes hydration products, and improves pore structure. CFRP confinement significantly increases compressive strength and ductility of the geopolymer concrete, and the LCA results demonstrate that the GO-modified CFRP composite achieves lower carbon emissions and competitive lifecycle costs compared to OPC-based systems.

Chapter 5 summarizes the key findings, emphasizing the technical feasibility and environmental benefits of integrating GO nanotechnology with geopolymer chemistry and CFRP confinement. The chapter concludes by offering recommendations for future research, including long-term durability studies, field-scale validation, and the incorporation of smart sensing technologies to monitor structural performance over time.

Chapter 2. Literature Review

The global cement and concrete industry is under increasing scrutiny due to its considerable environmental impact, with ordinary portland cement (OPC) production alone responsible for approximately 8 to 9 percent of global anthropogenic CO_2 emissions (Andrew, 2018). In this context, the development of alternative binder systems with lower embodied carbon and higher resource efficiency has emerged as a key research priority. Among these, alkali-activated materials (AAMs), and particularly fly ash-based geopolymers (FAGPR), offer a promising pathway toward sustainable infrastructure (Li et al., 2021a; Sumesh et al., 2017). These binders not only utilize industrial byproducts such as Class C fly ash (Li and Shi, 2025, 2020), blast furnace slag (Khater et al., 2013), and cement kiln dust (Ahmari and Zhang, 2013), but also avoid the energy-intensive calcination process inherent to OPC. Despite this potential, the widespread adoption of FAGPR has been hindered by several material and structural performance challenges (Singh et al., 2015), including low early-age strength, variable setting time, insufficient water resistance, and limited long-term durability under aggressive environmental conditions (i.e., cyclic freeze-thaw resistance).

To address these challenges, researchers have increasingly turned to using nanotechnology to mitigate these aforementioned disadvantages (Abdalla et al., 2022; Li et al., 2021a). Nanomaterials such as nano-silica (Han et al., 2022), carbon nanotubes (Su et al., 2020), and graphene-based derivatives (Huang and Sun, 2021), particularly graphene oxide (GO), have shown significant potential in enhancing the microstructure, hydration behavior, and durability of cementitious systems. GO is rich in oxygen-containing functional groups, which contribute to its high surface reactivity, dispersion capability in aqueous solutions, and chemical interaction with multivalent cations such as Ca^{2+} and Al^{3+}. These properties enable GO to promote the formation and cross-linking of C-(A)-S-H gels, refine pore structure, and reduce microcracking. Studies such as those by Xu et al. (Xu et al., 2018, 2019) and Li and Shi (Li and Shi, 2025, 2020) have shown that the inclusion of GO at a trace of dosages can lead to substantial improvements in compressive strength, shrinkage reduction, and freeze–thaw resistance. Advanced analytical techniques, including scanning electron microscopy (SEM), energy-dispersive X-ray spectroscopy (EDX), X-ray diffraction (XRD), thermogravimetric analysis (TGA), Fourier transform infrared spectroscopy (FTIR), and nuclear magnetic resonance (NMR), have been employed to verify the chemical and physical modifications induced by GO.

Beyond mechanical enhancement, GO has also been found to significantly influence the hydration kinetics and morphological development of geopolymer matrices. Its ability to act as a nucleation site accelerates gel formation and improves the degree of polymerization in aluminosilicate networks (Liu et al., 2020; Shamsol et al., 2024). Research has demonstrated that GO-modified binders exhibit improved resistance to water ingress and chemical degradation (Tang et al., 2024, 2023). FTIR and NMR spectra from freeze–thaw exposure tests reveal that GO slows the depolymerization of C-(A)-S-H gels and helps retain bound water within the matrix, thereby reducing the extent of microstructural damage

under cyclic loading (Li and Shi, 2025; Min et al., 2022). Moreover, the incorporation of GO has been shown to modify the interface transition zone (ITZ) between the binder and aggregates, which plays a crucial role in determining the overall durability and load-bearing behavior of hardened composites (Lu et al., 2022). GO not only enhances mechanical performance but also facilitates more uniform hydration product distribution and promotes greater chemical stability under environmental stress. GO-engineered FAGPR showed reduced calcium leaching and less degradation under freeze–thaw cycling (Li and Shi, 2025; Xu and Shi, 2020). Spectroscopic analyses confirmed more polymerized gel structures and better retention of structural water, which are key indicators of improved durability. These findings underscore the dual role of GO as both a physical nano-filler and a chemically active modifier in geopolymer systems.

While much progress has been made at the material level, the transition of GO-engineered FAGPR into structural applications remains limited (Hassan et al., 2020; Lahoti et al., 2019). One promising strategy for enabling this transition involves the use of carbon fiber-reinforced polymer (CFRP) tubes to provide external confinement. CFRP tubes are lightweight, corrosion-resistant, and capable of significantly enhancing the axial load-bearing capacity and ductility of confined concrete elements (Goonewardena et al., 2020; Zinkaah et al., 2022). Prior studies have demonstrated the mechanical benefits of CFRP-confinement in traditional and alternative concretes, including improved peak strength and post-peak ductility. However, the integration of GO-engineered FAGPR into CFRP-confined systems has received little attention, and the underlying mechanisms of interaction between the modified binder and CFRP shell remain largely uncharacterized. Integrating GO-modified geopolymers into CFRP-confined structural systems also offers opportunities to reduce the total volume of CFRP required, which can mitigate the embodied carbon and cost associated with advanced fiber composites. Several researchers have suggested that stronger, more durable core materials allow thinner confinement layers or more efficient stress transfer, yet few have empirically tested these interactions using GO-engineered binders (Alrshoudi et al., 2021). In this context, experimental and modeling work is needed to understand how material-level modifications influence structural-scale behavior, especially under multi-axial stress states and long-term loading conditions. These considerations are especially important for infrastructure applications where performance must be maintained over decades in variable climates.

Furthermore, there is a growing recognition that technical innovations in construction materials must be accompanied by environmental and economic assessments to ensure long-term viability (Salas et al., 2018; J. Zhao et al., 2021). Life cycle assessment (LCA) provides a structured framework to quantify environmental burdens, such as global warming potential (GWP), across the full life span of a material or system—from raw material extraction and processing to use and end-of-life. However, few studies have systematically evaluated the environmental performance of GO-engineered FAGPR or their CFRP-confined derivatives. Even fewer have incorporated structural function into the LCA functional unit, which limits the relevance of results for practical decision-making. Research by the present team has addressed this gap by coupling detailed experimental characterization with structural-scale

performance testing and LCA modeling. This allows for a cradle-to-grave comparison of different binder systems, accounting for both mechanical efficiency and environmental impacts.

In conclusion, the literature clearly demonstrates the technical promise of nano-engineered FAGPR and the potential benefits of CFRP confinement. GO emerges as a particularly effective nano-admixture, capable of improving both fresh and hardened properties of geopolymer binders while also enhancing resistance to environmental degradation. Nevertheless, significant knowledge gaps remain regarding the structural integration of these materials and their sustainability implications. This study responds to these gaps by investigating the GO-engineered FAGPR system from micro to macro scale, integrating it into CFRP-confined composites, and evaluating its life cycle performance to support its adoption in sustainable infrastructure development.

Chapter 3. Methodology

This chapter describes the experimental and analytical methods adopted to develop, characterize, and assess the proposed original alkali-activated fly ash-based geopolymer (FAGPR) and GO-engineered and FAGPR (GFAGPR), and their application in CFRP-confined structural composites. The methodology comprises material formulation, statistical design of experiments, macro- and micro-scale testing protocols and investigation, mechanical modeling, and life cycle assessment (LCA).

3.1 Materials

The primary binder component was Class C fly ash, sourced from a coal-fired power plant in Boardman, Oregon, USA. Its chemical composition was determined via X-ray fluorescence (XRF) and is reported in Table 3.1. The alkali activators included sodium silicate solution ($Na_2SiO_3 \cdot 9H_2O$) and calcium oxide (CaO), both of analytical grade and procured from Sigma-Aldrich. Sodium sulfate ($Na_2SO_4 \cdot 10H_2O$) was included to aid the reaction kinetics, and triisopropanolamine (TIPA) served as a non-chloride early-strength admixture. In addition, recycled glass powder (RGP) was used to densify and enhance the microstructure of the cementitious binder, while highly alkaline cement kiln dust (CKD) was incorporated to promote the hydration process in the alkali-activated binder. The chemical compositions of both materials are also provided in Table 3.1. To mitigate the negative effects of unburnt carbon in the fly ash, a commercial micro-vesicular fire suppressant (F500) was used at 3.75 wt% of fly ash.

Table 3.1. Chemical composition of fly ash and cement kiln dust (wt. %).

Chemical composition	Fly ash	CKD	RGP
SiO_2	28.62	14.69	50-55
Al_2O_3	16.75	6.53	14-20
CaO	28.13	41.4	20-25
Fe_2O_3	5.84	1.57	≤1
Na_2O+ K_2O	8.1	0.5	8-14
MgO	5.12	0.53	≤2
SO_3	7.22	0.49	/
Cr_2O_3	/	0.01	/
TiO_2	/	0.3	/
MnO	/	0.02	/
P_2O_5	/	0.05	/
Loss on ignition	1.5	33.1	≤0.5

Note: Loss on ignition (LOI) was measured by following the ASTM D7348-13: Standard Test Methods for Loss on Ignition (LOI) of solid combustion residues.

Graphene oxide (GO) was synthesized via a modified Hummers method and exhibited a specific surface area of ~2600 m^2/g. It contained approximately 71 wt.% carbon and 26 wt.% oxygen, with dominant functional groups including O–H, C=O, C=C, and C–O, as confirmed via X-ray photoelectron spectroscopy (XPS) and Fourier transform infrared spectroscopy (FTIR) (Figure 3.1). GO was dispersed ultrasonically into DI water to form a

2.5 g/L stable solution, which was then incorporated into the binder at 0.02 wt.% relative to fly ash.

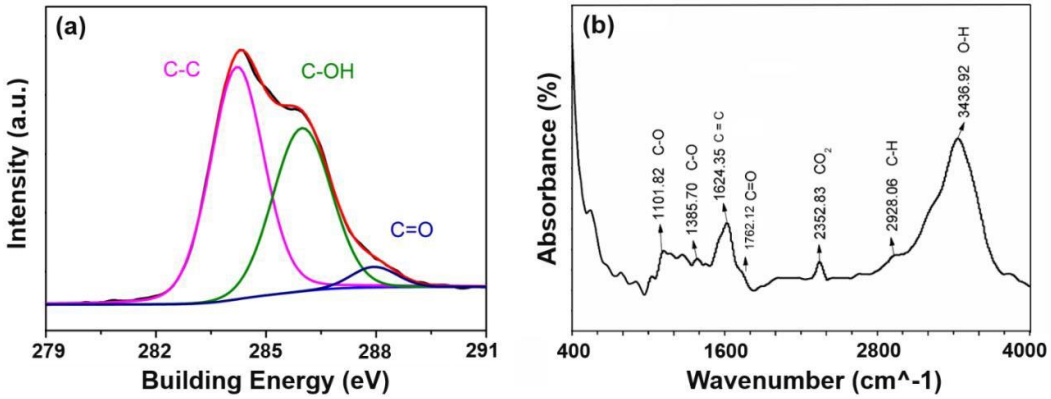

Figure 3.1. (a) XPS analysis and (b) FTIR analysis for GO **(Gong et al., 2024)**.

The coarse and fine aggregates used for (G)FAGPR concrete were crushed limestone and natural silica sand, respectively. A polycarboxylate-based high-range water reducer (HRWR) was added to enhance workability and facilitate GO dispersion. For structural confinement, CFRP tubes of various diameters and thicknesses were sourced from DragonPlate (NY, USA), with a tensile strength of ~4420 MPa and elastic modulus of ~234 GPa.

3.2 Statistical Design of Experiments

A Uniform Design (UD) approach was employed to investigate the effects of six binder constituents—sodium silicate (a.k.a. water glass: WG), recycled glass powder (RGP), calcium oxide (CaO), cement kiln dust (CKD), TIPA, and F500—on compressive strength at 7 and 28 days. Each factor was varied at four levels (Table 3.2), and 36 mix combinations were generated (Table 3.3). The water-to-binder ratio was fixed at 0.24, and GO and sodium sulfate dosages were held constant. A control sample without GO and a GO-modified target sample (with highest strength) were selected for further testing.

Table 3.2. The factors and their levels explored in the uniform design scheme.

Level	Factors					
	X_1 (WG)	X_2 (RGP)	X_3 (CaO)	X_4 (CKD)	X_5 (TIPA)	X_6 (F500)
1	0	0	0	0	0	0
2	2 wt.%	5 wt.%	1.2 wt.%	3 wt.%	0.6 wt.%	0.6
3	4 wt.%	10 wt.%	2.4 wt.%	6 wt.%	1.2 wt.%	1.2
4	6 wt.%	15 wt.%	3.6 wt.%	9 wt.%	1.8 wt.%	1.8

Table 3.3. The uniform design scheme used in this study.

Run No.	Factor X_1	Factor X_2	Factor X_3	Factor X_4	Factor X_5	Factor X_6
1	2	4	2	2	4	4
2	3	4	1	4	3	4
3	3	4	1	2	2	2

4	4	1	2	1	2	4
5	2	1	1	2	1	1
6	3	2	2	1	4	1
7	2	2	3	1	2	2
8	4	1	3	4	1	4
9	*4*	*1*	*4*	*1*	*3*	*2*
10	4	4	4	3	4	4
11	3	2	2	4	1	3
12	1	1	2	2	2	3
13	1	4	3	2	3	2
14	1	3	2	3	1	4
15	3	1	3	3	3	3
16	3	1	4	3	2	1
17	4	2	3	2	3	1
18	4	2	1	3	2	3
19	3	2	4	2	4	3
20	1	3	4	4	2	3
21	1	4	4	1	1	1
22	1	2	3	3	1	2
23	3	3	3	2	2	4
24	2	3	1	1	3	3
25	2	4	2	4	2	1
26	1	2	1	1	4	4
27	3	3	4	1	1	2
28	2	4	4	3	1	3

3.3 Fabrication of the Specimens

All (G)FAGPR paste specimens were prepared in the laboratory as follows. The Class C fly ash, sodium silicate, recycled glass powder, calcium oxide, and cement kiln dust were blended for 5 min without water to obtain a homogeneous mix. TIPA was dissolved in DI water for better dispersion before mixing with dry binder and this part of DI water was counted into the total water used to obtain fresh paste. Then, the remaining DI water, TIPA solution, 2.5g/L GO suspension, dry binders, and HRWR were blended together for another 5min to achieve the desired workability. After mixing, the fresh paste was cast into 5cm (diameter)×10 cm (height) cylinder molds, and all specimens were covered with plastic lid for 24 hours to avoid the water evaporation. Finally, the samples were demolded and cured in a wet chamber (22±2℃, relative humidity of 95±3%) for 6-day and 27-day for the 7-day and 28-day compressive strength test, respectively.

The process of fabricating concrete-filled CFRP tube specimens is detailed as follows. The bottom of the CFRP tubes was sealed using tailored corrugated paper and waterproofing tape (Figure 3.2). Fine aggregate, coarse aggregate, water, and HRWR were blended in the mixer for 3 min, then the dry binder was fed into the mixer and followed another 5 min blending to achieve promising workability. The mixture proportions for OPC, FAGPR, and GFAGPR concretes are presented in Table 3.4. Subsequently, the fresh concrete was poured into the tubes and subjected to vibration to eliminate any entrapped air bubbles within the

mixture. A plastic film was employed to cover the surface of the specimens, preventing water evaporation. No additional curing was required for this composite material. Furthermore, unconfined cylindrical concrete specimens with dimensions of 10 cm (diameter) × 20 cm (height) were also fabricated accordingly for providing information of unconfined compressive strength (f'_{co}). After 24-hour curing, these unconfined specimens were demolded and subjected to 27-day curing process at a temperature of 22 ± 2 °C and a relative humidity of 95 ± 3%. Due to unforeseen technical issues, all the specimens were tested after 3 months instead of the intended 28-day age.

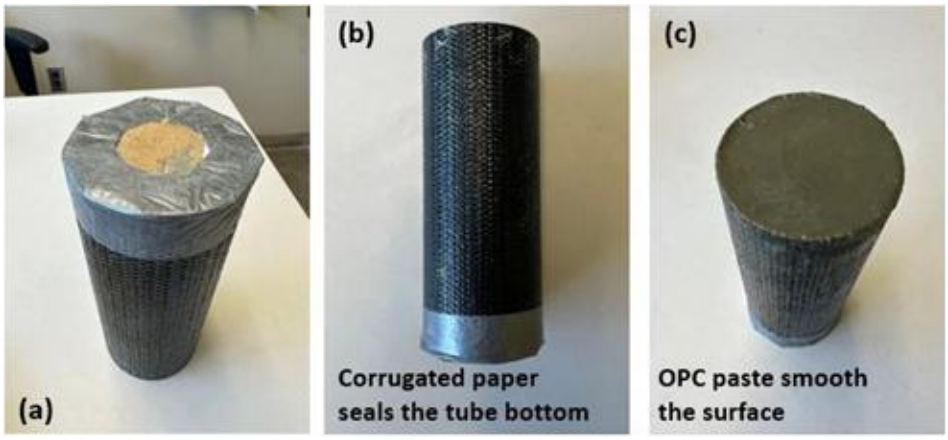

Figure 3.2. The process of preparing CFRP tube for fabricating concrete-filled CFRP tube composite.

Table 3.4. Mixture Proportion of OPC And (G)FAGPR Concretes

Type	Binder (kg/m^3)	Water (kg/m^3)	Fine aggregate (kg/m^3)	Coarse aggregate (kg/m^3)	HRWR (kg/m^3)
OPC	540	180	811	1120	1.2
FAGPR	630	190	635	935	9.6
GFAGPR	630	190	635	935	9.6

3.4 Mechanical Testing

Compressive strength was measured in accordance with ASTM C109 using cylindrical specimens (50 mm × 100 mm). Both 7-day and 28-day compressive strengths were recorded. For CFRP-confined composite testing, larger cylindrical specimens (with varied diameter: D, height: H, and thickness: T) were fabricated and tested under axial compression using an Instron 5900 multi-station system at a loading rate of 2 mm/min, following ASTM C1231/C1231M. Strain gauges were installed to monitor CFRP deformation during failure.

The unconfined compressive strength (f'_{co}) and the confined compressive strength (f'_{cc}) of each composite specimen were determined. Mechanical response was analyzed using established CFRP confinement models per ACI 440.2R, including the calculation of confinement pressure and strain efficiency factors.

3.5 Macroscale Property Evaluation

The macro-level engineering properties of the (G)FAGPR pastes were evaluated to

assess the fresh behavior, dimensional stability, and water resistance of the binder system. Workability was tested using a mini-slump cone method, where the spread diameter of the fresh paste was recorded to reflect flowability. The setting time was measured using a concrete pocket penetrometer following ASTM C403. Dimensional stability was assessed via the linear shrinkage of prismatic paste specimens (25 mm × 25 mm × 250 mm) over a 28-day curing period, following the guidelines in ASTM C596.

Water absorption behavior was studied using ASTM C1585, in which cylindrical disc specimens (50 mm in diameter and 20 mm in height) were dried, sealed, and partially immersed in deionized water to monitor capillary absorption over time. The water absorptivity coefficient (k) can be calculated using the following formula:

$$I = \frac{m_t}{a \times b} = k\sqrt{t} \tag{3.1}$$

where I is the absorption, m_t is the change in specimen mass in gram at time t, a is the exposed area of the specimen (mm^2), b is the density of the water (10^{-3} g/mm^3), k is the absorptivity coefficient, and t is the time (s).

All tests were conducted at consistent laboratory conditions, and each property was evaluated with at least three replicate specimens for statistical reliability.

3.6 Microstructural and Chemical Characterization

To elucidate the hydration mechanisms and microstructure of (G)FAGPR pastes and the microstructural evolution of the (G)FAGPR pastes before and after freeze–thaw cycling, a comprehensive series of spectroscopic and microscopic characterization techniques was employed. Scanning Electron Microscopy (SEM) equipped with Energy Dispersive X-ray Spectroscopy (EDS) was used to observe micromorphology and elemental distribution across selected cross-sections. Crystalline phase changes were examined via X-ray Diffraction (XRD) using Cu Kα radiation (λ = 1.54 Å), with diffraction patterns compared across different hydration ages and freeze–thaw exposure states. Thermogravimetric Analysis (TGA) was performed using a PerkinElmer PYRIS 1 analyzer from 50°C to 800°C at a constant heating rate of 10°C/min to quantify mass loss associated with moisture evaporation, ettringite decomposition, portlandite decomposition, and carbonate formation. Fourier Transform Infrared Spectroscopy (FTIR) was carried out using the KBr pellet method (1:100 mass ratio of sample to KBr) in the 400–4000 cm^{-1} range at 4 cm^{-1} resolution to identify key functional groups and analyze the degree of polymerization in the aluminosilicate network. Solid-state Nuclear Magnetic Resonance (NMR) spectroscopy was conducted on a Varian DD2 600 MHz instrument at 7.05 T to capture the structural evolution of Si and Al species in the geopolymer gels. These techniques were jointly applied to both (G)FAGPR paste specimens and their aged counterparts before and after exposure to freeze–thaw cycles, enabling a detailed comparison of chemical composition, hydration behavior, and structural ordering.

3.7 Life Cycle Assessment (LCA)

A cradle-to-grave life cycle assessment (LCA) was conducted to evaluate and compare

the environmental and economic impacts of OPC, FAGPR, and GFAGPR concrete systems, with and without CFRP tube confinement. The LCA framework followed ISO 14040 and 14044 standards and included goal and scope definition, life cycle inventory (LCI), life cycle impact assessment (LCIA), and interpretation (**Figure 3.3**). The functional unit was defined as structural columns with comparable load capacity (~6000 kN) operating under the same service environment (Pullman, WA), enabling a performance-equivalent comparison. System boundaries encompassed raw material production (e.g., fly ash, OPC, CFRP), concrete batching and casting, transportation, maintenance, and end-of-life treatment, including potential recycling of CFRP components. Inventory data were collected from a combination of commercial databases (e.g., Ecoinvent), peer-reviewed literature, industry reports, and laboratory-measured values. The LCIA focused primarily on Global Warming Potential (GWP), expressed in kg CO_2-equivalent, as the environmental impact indicator. Economic cost analysis was conducted in parallel based on unit price data for materials, production energy, transportation distances, and labor. All inputs and outputs were normalized to the functional unit, and sensitivity analysis was performed to test key parameter assumptions. The final LCA model enabled quantitative comparison between different concrete types and structural configurations, highlighting trade-offs between environmental footprint, material performance, and cost.

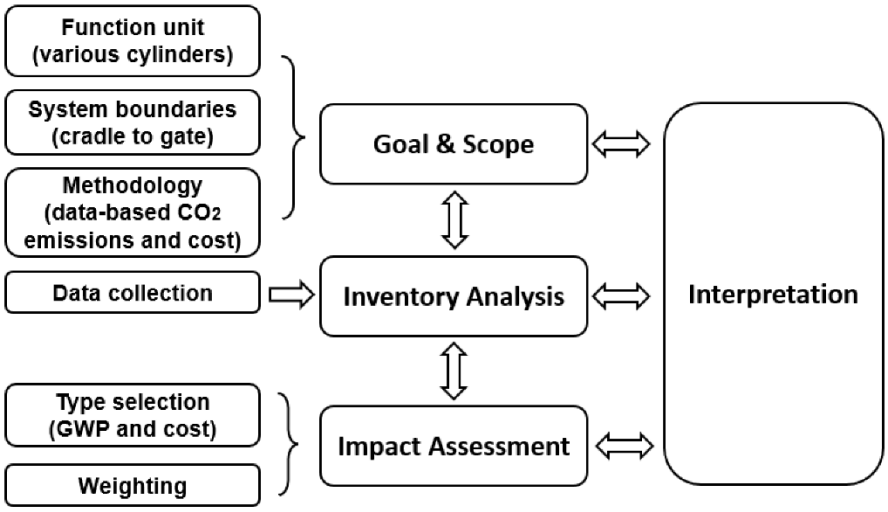

Figure 3.3. The Framework of LCA model in this study

Chapter 4. Results and Discussion

This chapter presents and analyzes the results obtained from the experimental and modeling work conducted on the (G)FAGPR pastes and their application in CFRP tube-confined structural composites. The findings are organized to reflect a multiscale evaluation, from macro-level mechanical performance and freeze–thaw durability to microstructural mechanisms and structural-scale behavior, culminating in an integrated life cycle assessment.

4.1 Compressive Strength of GFAGPR Paste

The compressive strength (CS) of these 36 GFAGPR pastes was tested, and the results are presented in Table 4.1. Among these samples, the No.9 GFAGPR specimen demonstrated the highest mechanical properties.

Table 4.1. Compressive strength of GFAGPR paste specimens (MPa)

Run No.	CS 7d	CS 28d	Run No.	CS 7d	CS 28d
1	8.70	11.03	19	9.27	11.34
2	/	/	20	8.61	9.16
3	5.36	7.25	21	7.12	17.82
4	8.97	10.24	22	8.88	10.95
5	6.57	6.88	23	6.55	8.19
6	10.90	16.00	24	1.26	1.86
7	10.06	15.80	25	5.30	11.73
8	9.41	13.89	26	5.02	6.00
9	13.40	29.14	27	9.32	12.99
10	8.49	11.50	28	8.25	10.23
11	4.89	5.61	29	9.15	16.74
12	6.30	7.21	30	5.59	6.39
13	7.14	7.93	31	8.08	12.76
14	4.09	5.16	32	5.30	6.59
15	7.45	10.17	33	5.54	7.52
16	9.84	14.73	34	8.32	10.54
17	8.45	11.93	35	8.30	9.56
18	6.86	8.87	36	6.87	8.01

Note: Sample No.2 exhibited rapid hardening and could not be cast into the mold.

Multi-regression analysis was employed to correlate the CS_{7d} and CS_{28d} with these six parameters, and two predictive equations were established as follows:

$$CS_{7d} = 5.09 + 0.88\,X_1 - 0.58\,X_2 + 2.91\,X_3 - 0.25\,X_1X_2 - 0.34\,X_1X_6 + 0.04\,X_2X_4 + 0.27\,X_2X_5 - 0.19\,X_3X_4 - 0.66\,X_3X_5 + 0.47\,X_3X_6 \quad (4.1)$$

$$CS_{28d} = 9.26 + 4.70\,X_3 - 1.36\,X_4 + 3.59\,X_5 - 6.69\,X_6 + 0.47\,X_1X_6 - 0.23\,X_2X_3 + 0.07\,X_2X_4 - 1.30\,X_3X_5 + 0.78\,X_4X_6 \quad (4.2)$$

The predicted values agreed well with the experimental values. The R-square was 0.80 and 0.75 for CS_{7d} and CS_{28d}, respectively. Furthermore, the *p* value was $4.66e^{-6}$ and $1.25e^{-5}$ for CS_{7d} and CS_{28d}, both of which were greatly smaller than 0.05, suggesting that these predictive models are highly reliable. In addition, these models also could be used to illustrate the synergetic effect of the six parameters on the strength property, and these interactions were revealed and presented in following Figures. The three-dimensional (3D) contour plots (as shown in the left) were used to show the change of CS_{28d} with variation of two selected parameters while other factors fixed at a medium level. A corresponding contour map (as shown in the right) was also supplied to facilitate the understanding.

Figure 4.1 shows that the CS28d increased with the use of lower F500 content and a higher waterglass dosage when the other factors were fixed at a medium level. The strength enhancement induced by waterglass is due to the role of waterglass as an effective activation agent of fly ash (Xie and Xi, 2001). The negative coefficient (−6.69) of F500 (X6), F500 was not very beneficial to the compressive strength of the FAGPR pastes in this study, which is likely due to the undesirable impact of excessive F500 on the hydration of alkali-activated fly ash etc.

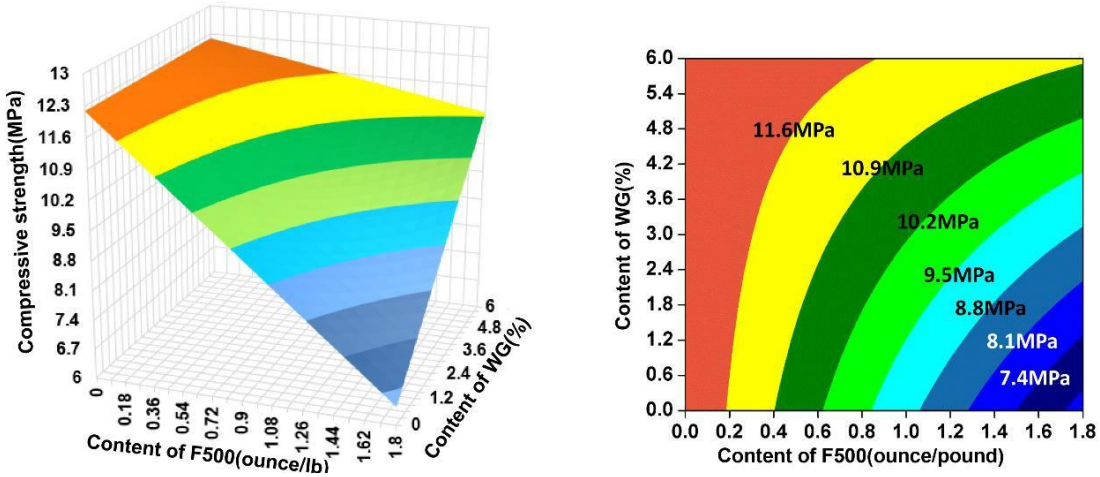

Figure 4.1. Relationships between 28-day compressive strength, WG dosage, and F500 dosage (with 7.5% RGP, 1.8% CaO, 4.5% CKD and 0.9% TIPA)

Figure 4.2 reveals that the CS28d increased with the growth of CaO content while the dosage of RGP was at a low level, which could be explained by the alkali-activated effect of CaO. However, when the content of RGP ranged from 12 wt.% to 15 wt.%, there was no obvious relationship between compressive strength and the growing content of CaO. This could be explained by the limited pozzolanic reactivity of RGP and large amount of unreacted RGP that would break the microstructure of hydration products. Similar conclusions were also demonstrated by Schwarz and Matos (Matos and Sousa-Coutinho, 2012; Schwarz and Neithalath, 2008).

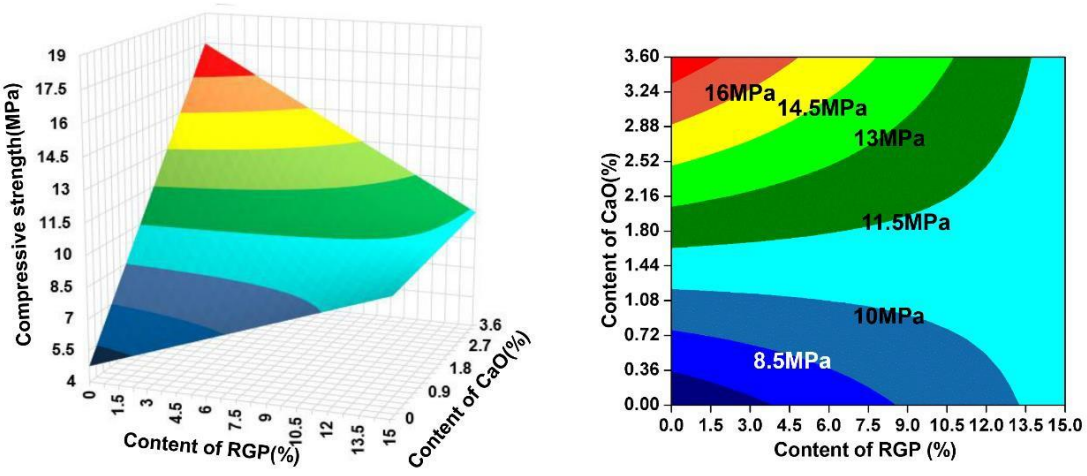

Figure 4.2. Relationships between 28-day compressive strength, RGP dosage, and CaO dosage (with 3% WG, 4.5% CKD, 0.9% TIPA and 5.625% F500).

Figure 4.3 suggests a complex interaction between RGP and CKD, with the CS28d slightly increased with the rise in CKD content when the RGP content was at a high level. This could be attributed to the activation of RGP by the highly alkaline CKD, leading to increased product hydration and enhanced strength. However, when the RGP content was at a low level, the CS28d decreased with the increase in CKD content. This phenomenon can be explained by the high free-CaO content (up to 41.4 wt.%) present in CKD, which may lead to poor soundness and thus a reduction in compressive strength (Wang et al., 2017).

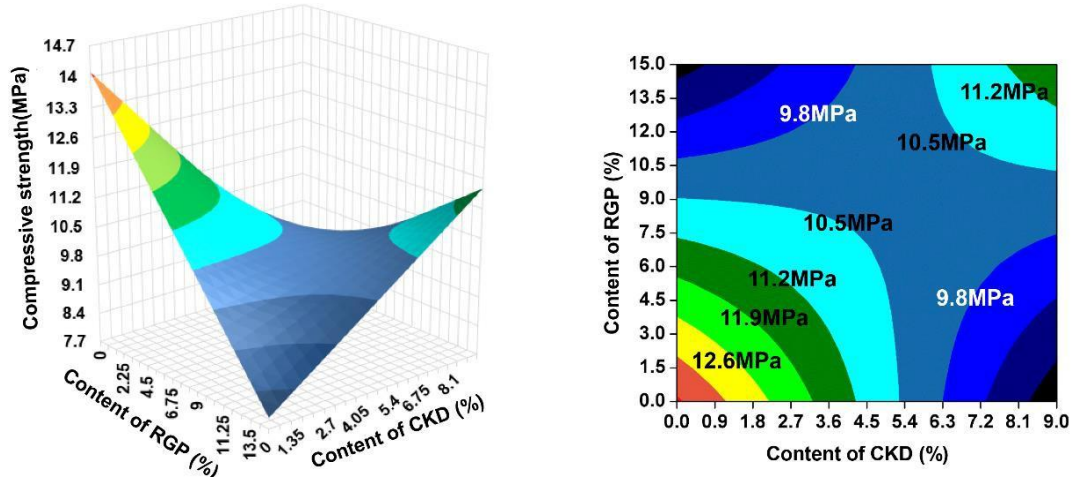

Figure 4.3. Relationships between 28-day compressive strength, RGP dosage, and CKD dosage (with 3% WG, 1.8% CaO, 0.9% TIPA and 5.625% F500).

4.2 Freeze-thaw resistance of (G)FAGPR paste

Figure 4.4 illustrates that GO significantly improved the residual compressive strength of the GFAGPR paste specimens over the freeze/thaw cycles. Compared with GFAGPR, FAGPR was more sensitive to the cyclic F/T action, as confirmed by the quick degradation of strength with the increase in F/T cycles. As shown in **Figure 4.4**, the strength

of GFAGPR paste specimens slightly increased between 10~20 cycles, which might be attributed to the continuing hydration of GFAGPR enabled by GO and thus slightly improved the compressive strength. This phenomenon was also observed in our previous research work regarding the F/T resistance of fiber-reinforced-plastic (FRP) wrapped concrete samples (Lei et al., 2021), in which the compressive strength increased by about 15% in the first 15 F/T cycles. At around 48 F/T cycles, only about 6% decrease in compressive strength of GFAGPR paste was observed while the strength of FAGPR was seriously degraded by about 33%. This result agreed well with many other researchers' studies regarding the nano-engineered geopolymer composites. For example, our previous work demonstrated that the admixed GO significantly improved the F/T resistance of GFAGPR pervious concrete (Xu and Shi, 2020). Shahrajabian and Behfarnia reported that nano-SiO_2, nano-Al_2O_3, and nano-clay effectively reduced the compressive strength loss of alkali-activated slag GPR concrete during F/T cycles (Shahrajabian and Behfarnia, 2018). Wang et al. also reported that nano-SiO_2 benefited the F/T resistance of metakaolin-fly ash-based geopolymer mortar (K. Wang et al., 2021).

The enhanced residual compressive strength observed in the presence of GO cannot solely be attributed to the outstanding mechanical properties of GO sheets, which possess a Young's modulus of approximately 0.3 TPa and an intrinsic strength of 112 GPa, allowing them to act as crack-bridging agents and resist tension, and thus mitigating crack propagation (He et al., 2018). More importantly, the beneficial interactions between the functional groups present on the GO and the cementitious matrix greatly contribute to the observed improvement in compressive strength. This improved microstructure helps mitigate moisture migration within the FAGPR composite. Our previous work confirmed that GO reduced the water absorption coefficient of FAGPR by 43%. Additionally, GO decreased the surface hydrophilicity of FAGPR, leading to an 87.5% increase in the water contact angle (Li and Shi, 2020). This effect may be attributed to GO inducing the formation of nano/micro-scale hydrates, thereby creating a mixed nano/micro hydrophobic structure (Li and Shi, 2022). The synergistic effect of reduced water absorption and increased water contact angle contributes to enhancing the F/T resistance of GFAGPR. The following section will focus on the beneficial role of GO in the GFAGPR hydration system before and after F/T cycles. The following advanced microscopic analysis sections will focus on the advantageous roles played by GO in this GFAGPR hydration system, both before and after F/T cycles.

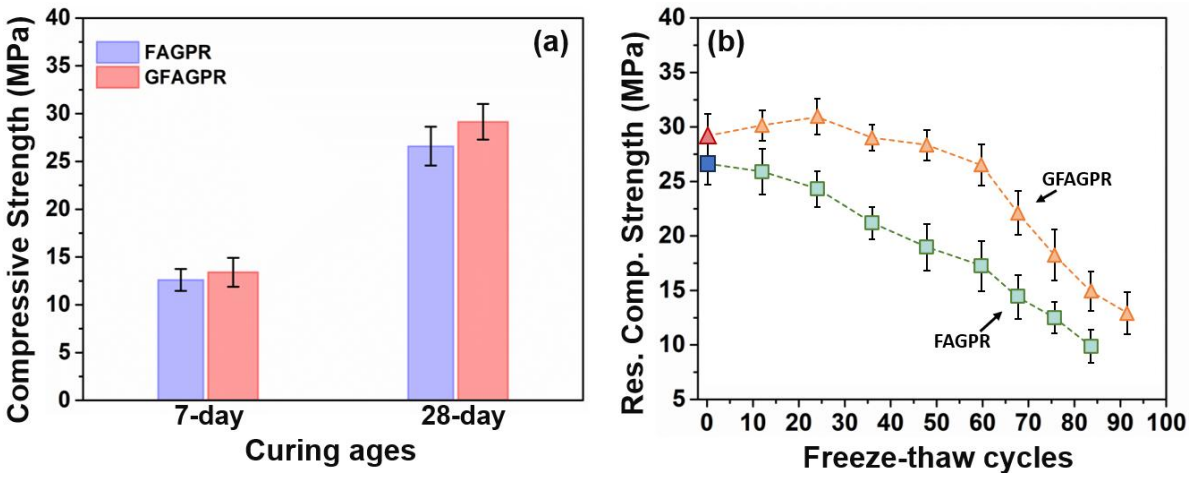

Figure 4.4. (a) Compressive strength of FAGPR and GFAGPR at 7-day and 28-day, respectively; (b) Compressive strength of FAGPR and GFAGPR at different freeze-thaw cycles.

4.3 GO's influence on (G)FAGPR Paste: Macroscopic Perspective

4.3.1 Setting Time and Workability Analysis

The setting time and workability performance of the selected GFAGPR and FAGPR samples were tested, and the presence of GO influenced both properties. The setting time for the GFAGPR sample was approximately 7 minutes, which was slightly faster than the FAGPR sample that took about 8 minutes to set. Several other researchers have also reported similar conclusions regarding the influence of GO on setting time in various cementitious materials. For example, Lu et al. (Lu et al., 2017) indicated the setting time of OPC paste decreased from 205 minutes to 142 minutes by incorporating 0.08 wt.% GO, and final time decreased from 285 minutes to 224 minutes. Mohammed et al. (Mohammed et al., 2017) demonstrated that the presence of GO nanosheets reduced the initial setting time of OPC paste from 160 minutes to 120 minutes. They concluded that the GO accelerated the hydration process of cementitious binder and thus led to a shorter setting time. It is noteworthy that the setting time of (G)FAGPR paste was considerably shorter than that of OPC paste. This phenomenon could be attributed to the substantial amounts of alumina and the strong alkali-activation reaction present in the (G)FAGPR paste.

For workability, the diffused area in this study was 161.4 mm × 156.76 mm in the FAGPR paste sample which indicates better workability than that of the GFAGPR sample (139.8 mm × 136.6 mm). This reduction also aligned with Lu's research, which demonstrated a 24% decrease in fluidity upon adding 0.08 wt.% GO (Lu et al., 2017). The most widely accepted explanation for this reduction is that nanoparticles, like GO, possess a large specific surface area and higher surface energy, leading them to absorb more water and consequently decrease workability. Additionally, the accelerated hydration process induced by GO can also impact workability, further contributing to the observed changes in setting time and fluidity.

4.3.2 Volume Change Analysis

Volume change of selected GFAGPR and FAGPR samples was recorded, and the results are presented in Figure 4.5. The significant increase in length observed in both samples is in contrast to the typical observation of volume shrinkage in alkali-activated fly ash systems. For example, Lee et al. (Lee et al., 2014) observed the shrinkage behaviors in alkali-activated fly ash/slag (AFS) binder and indicated that the chemical shrinkage of the AFS paste was lower than that of the OPC paste. However, in contrast, the autogenous shrinkage of the AFS paste was higher than that of the OPC paste. The main reason for the unusual expansion in this study might be attributed to the comparatively higher content of SO_3 (as high as 7.22 wt.%), and CaO (as high as 28.13 wt.%) in fly ash while the SO3 content was only 0.61 wt.% and CaO content was only 6.26 wt.% in Lee's research. In addition, the extra-added CaO and Na_2SO_4 used to alkali-activate fly ash would react with more Al3+ and generate more expansive gypsum and ettringite to expand the volume. The presence of gypsum and ettringite was verified by TGA and XRD in the later discussion. Although the volume of both GFAGPR and FAGPR samples expanded, the difference between them was insignificant. In light of the short setting time, this kind of (G)FAGPR binder was well-suited for certain applications that demand rapid setting and fast strength development in cementitious materials. Furthermore, due to its significant expansive properties, this (G)FAGPR could be utilized to prepare self-stressed steel tubular concrete or concrete- filled carbon-fiber reinforced plastic tube (CFRP) composite without the need for additional expansive agents.

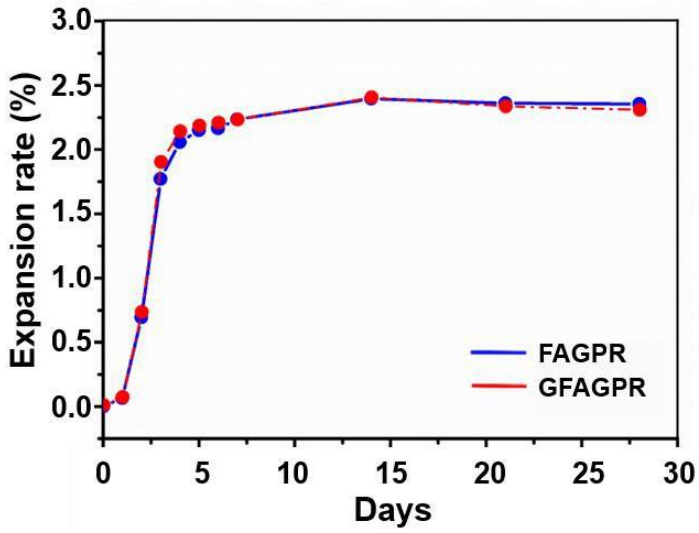

Figure 4.5. Volume expansion of GFAGPR and FAGPR paste samples.

4.3.3 Water Absorption

The changes in the water absorption character induced by GO were explored and the results are presented in Figure 4.6, which depicts the water absorption over time for selected GFAGPR and FAGPR paste samples. It was clear that the water absorption increased sharply during the first 0.5 hours and then remained stable until the finish. The

water absorptivity coefficient k of these two samples was calculated by linear fitting; *k* of the GFAGPR and FAGPR samples were 0.0834 mm/s^1/2 and 0.1451 mm/s^1/2 (decreased by 43%), respectively. Similar results also obtained by Mohammed et al.(Mohammed et al., 2015), who demonstrated that water absorption of cement paste was decreased from 7.3% to 6.5% by incorporating with 0.03 wt.% GO. These findings collectively support the notion that GO can serve as an effective additive to significantly reduce the water absorption of FAGPR paste. This enhanced water resistance makes GFAGPR binder a promising candidate for various construction applications requiring improved durability and reduced water permeability.

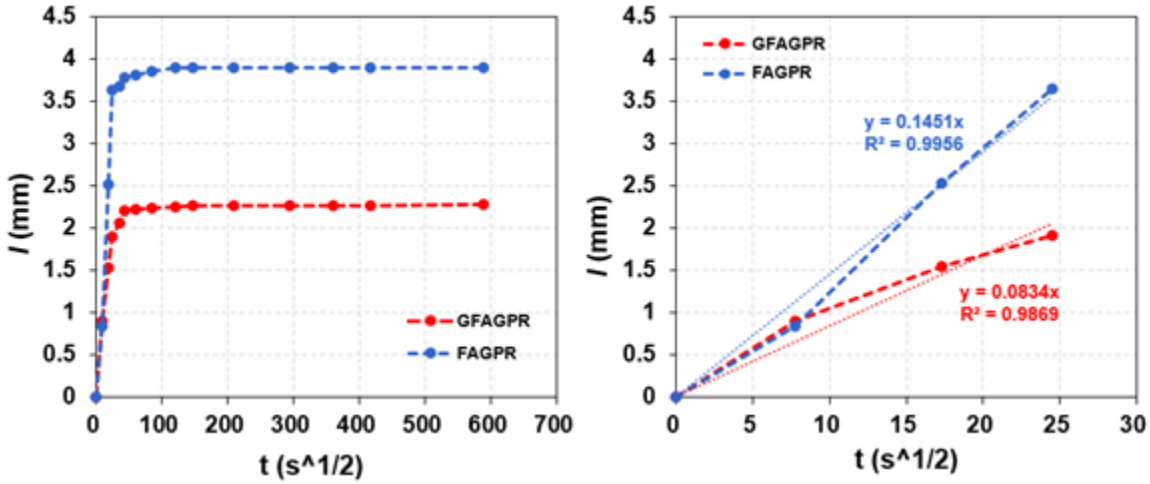

Figure 4.6. Evaluation of water absorption of the selected pastes: (a) overall trend; (b) linear range.

4.4 GO's influence on (G)FAGPR Paste: Microscopic Perspective

4.4.1 X-ray Diffraction Analysis

Figure 4. 7 illustrates a comparison of the XRD patterns of selected paste specimens before and after F/T cycles, revealing the influence of GO on the change of crystalline phases in hydrates. Four specimens were selected, namely FAGPR and GFAGPR before and after 84 F/T cycles, denoted as FAGPRB, GFAGPRB, FAGPRA, and GFAGPRA, respectively. As previously discussed (Li and Shi, 2020), the main crystalline phases in FAGPRB and GFAGPRB were Mullite (M) at approximately 25°, 33°, 41°, and 43°, Quartz (Q) at approximately 27°, 37°, and 47°, Ettringite (E) at 23°, Cubic tricalcium aluminate (CA) at 34°, Gypsum (G) at 28°, and Portlandite (CH), although some of them were too weak to be marked in **Figure 4.7**. However, calcium carbonate (C) was more dominant in FAGPRA and GFAGPRA, likely due to the airborne CO_2-induced carbonation in the aged FAGPRA and GFAGPRA pastes during the F/T process and sample preparation for microscopic investigation. The presence of calcium carbonate was also confirmed by TG/DTG and FTIR analysis, detailed in later sections.

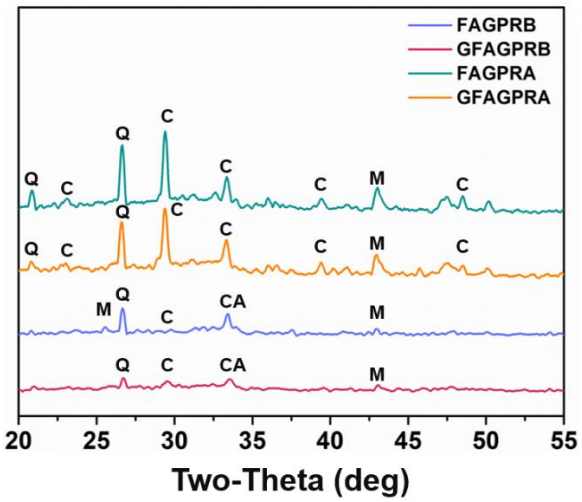

Figure 4.7. XRD patterns for FAGPRB, GFAGPRB, FAGPRA, and GFAGPRA, respectively.

4.4.2 Thermogravimetric and Differential Thermogravimetric Analysis

The TG/DTG analysis provides mechanistic insights into the effect of GO on the hydration of FAGPR before and after exposure to the cyclic F/T process. In our previous work, we have reported the results of TG/DTG analysis for FAGPRB and GFAGPRB, as also shown in **Figure 4.8**. The first mass loss observed between 25°C to 150°C is attributed to moisture evaporation, Ettringite decomposition (around 100°C), AFm decomposition (around 150°C), and C-S-H/C-A-S-H gel dehydration (Williams et al., 2002; Winnefeld et al., 2010). The second mass loss observed in FAGPRB between 350°C to 450°C is due to the decomposition of portlandite. However, no obvious portlandite was detected in GFAGPRB, indicating that the admixed GO facilitated more efficient hydration, resulting in the consumption of more portlandite than in FAGPR. The third mass loss occurred between 600~750°C, mainly because of the decomposition of the carbonate phase (calcite).

After exposure to F/T cycles, the chemical composition of FAGPR and GFAGPR changed. The first mass loss observed between 50°C to 200°C in both FAGPRA and GFAGPRA was still attributed to moisture evaporation, AFt/AFm decomposition, and C-S-H/C-A-S-H gel dehydration. Nonetheless, this overlapped peak differs from the one in **Figure 4.8a**, suggesting a change in the proportion of these phases after F/T cycles. No obvious portlandite was detected in **Figure 4.8b**, indicating that portlandite was continuously consumed or leached out during the F/T process. The mass loss between 500°C to 800°C is attributable to the change of carbonate phase, which not only involved the decomposition of calcite but also the transition from aragonite to calcite (Tone and Koga, 2021). Although both aragonite and calcite belong to calcium carbonate, unstable aragonite is orthorhombic crystal systemic and mainly come from carbonated C-S-H/C-A-S-H gels while stable calcite is trigonal crystal systemic and mainly comes from carbonated portlandite. The TG/DTG analysis also suggests that GO prevented the generation of aragonite, in other words, GO improved the carbonation resistance of hydrate gels. A similar

conclusion has been reported in our previous research with a focus on the influence of GO on a ternary limestone clay cement paste (Gong et al., 2024).

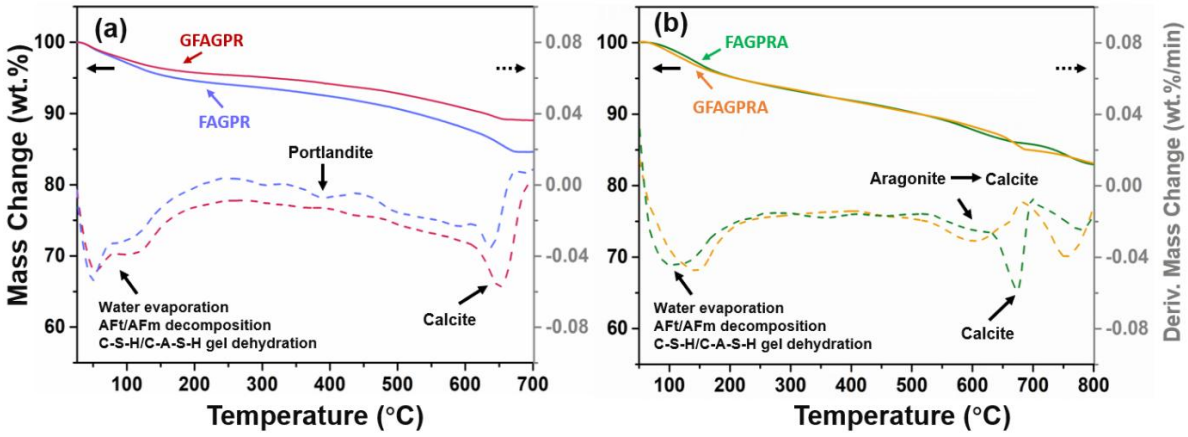

Figure 4.8. TG/DTG analysis for (a) FAGPRB and GFAGPRB; and (b) FAGPRA and GFAGPRA, respectively.

4.4.3 Fourier-Transform Infrared Spectroscopy Analysis

Following TG/DTG analysis, Fourier transform infrared spectroscopy (FTIR) analysis was carried out to illustrate the influence of GO on the phase change and chemical arrangement in the hydrated paste, before and after F/T cycles, respectively (see **Figure 4.9**). The overlapped peak of Si-O stretching and Si(Al)-O stretching in **Figure 4.9b** indicates the presence of low-polymerized Si-O (like Q0~2 as detailed in later NMR analysis) tetrahedron in C-S-H gel (at around 900-1250 cm-1) and C-A-S-H gel (shoulder peak at around 1100 cm-1), respectively (Gong et al., 2022; Kumar et al., 2017). The intensity of these peaks, i.e., their transmittance (%), can be used to indirectly describe the hydration reactivity of raw materials (such as fly ash) and the hydration polymerization degree of the hydrated binder. A stronger peak indicates more low-polymerized Si-O tetrahedrons and thus higher reactivity of the raw material while implies the lower polymerization degree of the hydrated binder (Li et al., 2021b). In this study, the peak intensity of low-polymerized Si-O tetrahedron in GFAGPRB paste sample was relatively lower than that in FAGPRB paste sample, suggesting that the admixed GO enabled the transition from low-polymerized Si-O tetrahedron to high-polymerized Si-O tetrahedron (like Q3~4 as detailed in later NMR analysis), i.e., GO improved the polymerization degree of hydrates. This conclusion was also verified by SEM/EDS and NMR analysis in later sections. Similar results were obtained after exposure to F/T cycles, in which GFAGPRA showed a higher polymerization degree than FAGPRA, suggesting GO mitigated the degradation of hydrates during the F/T cycles, which also helped to explain the higher residual compressive strength of GFAGPRA. It is worth noting that although the Si-O peak intensity in GFAGPRA (FAGPRA) was lower than that in GFAGPRB (FAGPRB), the polymerization degree of GFAGPRA (FAGPRA) was still found to be lower than GFAGPRB (FAGPRB), as confirmed by EDS and NMR analysis later. This can be attributed to the leaching out of many Si-based components during the F/T process, which led to a lower intensity of the Si-O peak.

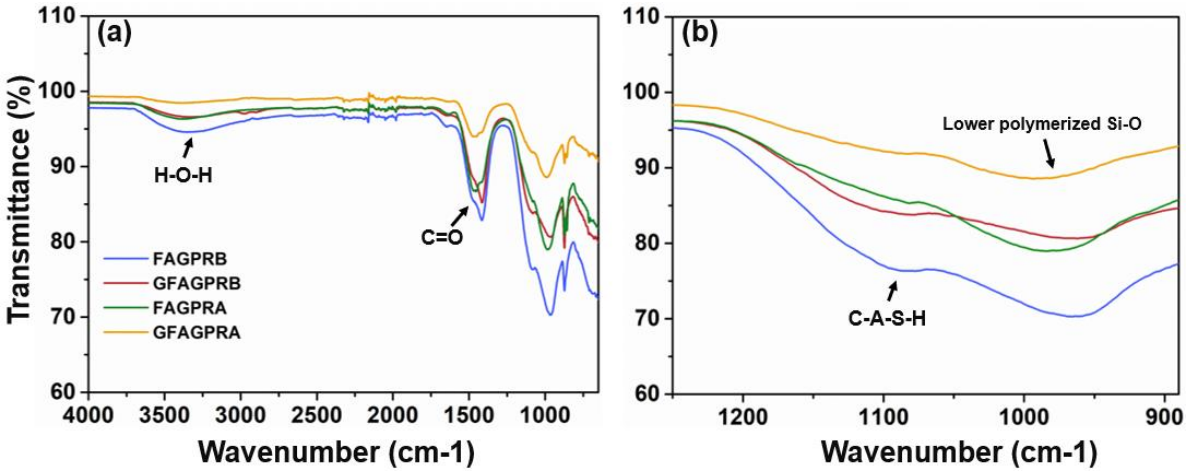

Figure 4.9. FTIR patterns for FAGPRB, GFAGPRB, FAGPRA, and GFAGPRA from (a) 4000~650cm-1 and (b) 1250~880 cm-1, respectively.

4.4.4 Scanning Electron Microscope Analysis

The difference of microstructure induced by GO nanosheets between the GFAGPR and FAGPR paste samples was examined by SEM, and the results are presented in **Figure 4.10**. At a magnification of 1000 times, dissolved fly ash particles were observable in the GFAGPR sample, while the FAGPR sample exhibited several micro-cracks. Furthermore, at a magnification of 3000 times, the microstructure of the GFAGPR sample appeared more homogeneous and integrated compared to the FAGPR sample, which showed numerous pores and gaps between particles. These observed differences in microstructure could aid in explaining the variation in compressive strength between the two samples

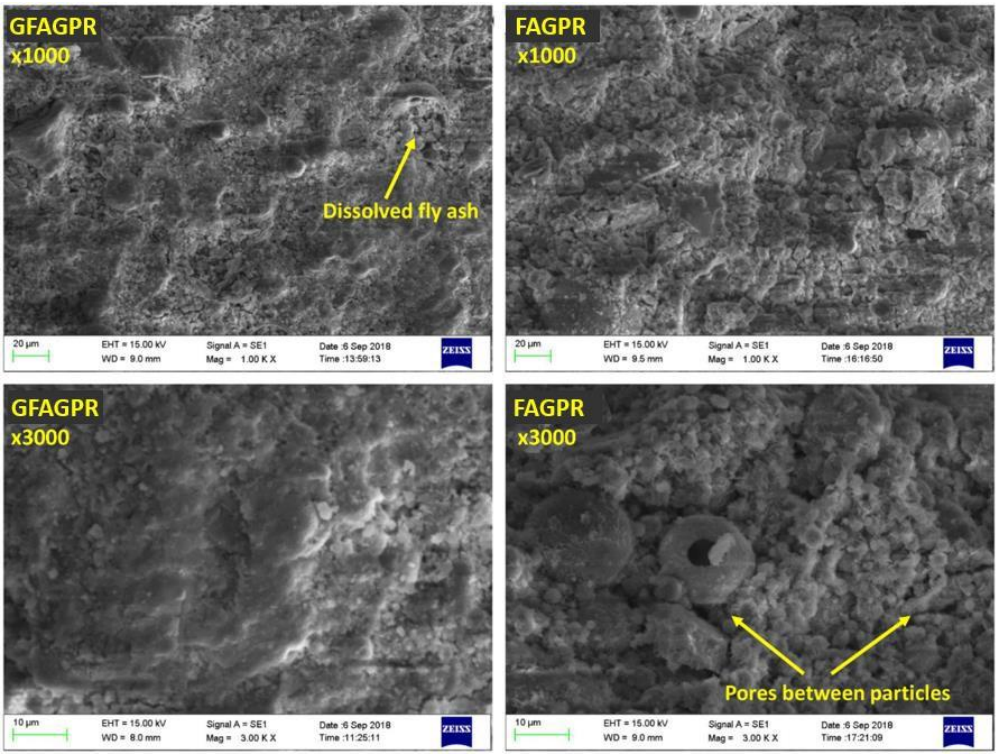

Figure 4.10. Difference between the microstructure of the selected GFAGPR and FAGPR paste sample

Figure 4.11 reveal that the admixed GO maintained the microstructure integration of GFAGPRA paste during the cyclic F/T process. This result is consistent with our previous work, where we found that GO promotes a more homogenous and integrated microstructure in GFAGPR through its nano-filler, crack-bridging, crack-confinement, hydration-acceleration, and template-polymerization effects.

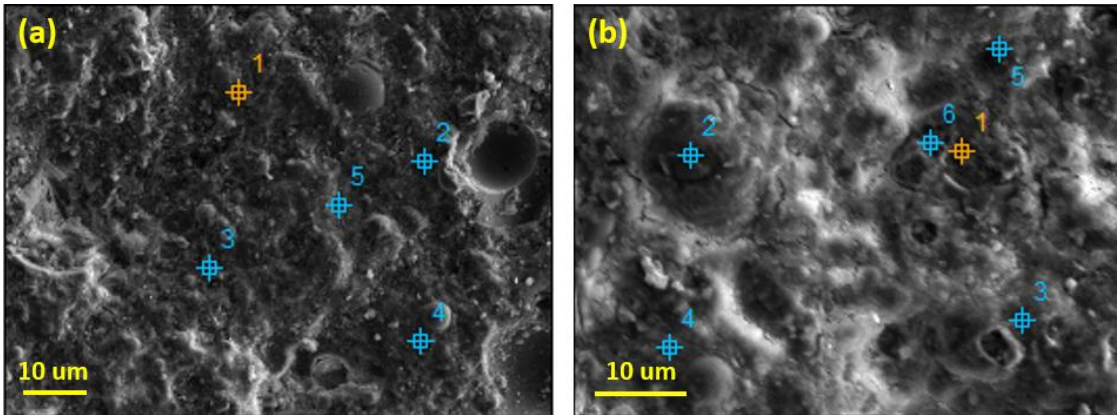

Figure 4.11. Microstructure of (a) GFAGPRA and (b) FAGPRA at 84 F/T cycles.

4.4.5 Energy Dispersive Spectroscopy Analysis

Figure 4.12 demonstrates the positive effects of GO on controlling the distribution of key elements (Ca and Al) in GFAGPR before and after exposure to F/T cycles. Our previous

research has shown that the introduction of GO resulted in a higher relative concentration of sampled Ca ions but a lower relative concentration of sampled Al element in light of the electronegative GO nanoplatelets attracting Ca cations while repelling Al ions in the form of $Al(OH)_4^-$ (Li et al., 2022; Li and Shi, 2020; Xu et al., 2019). These trends were also observed after exposure to F/T cycles. As shown in **Figure 4.12a**, both GFAGPRB and GFAGPRA had a higher relative concentration mean of Ca compared to FAGPRB and FAGPRA, respectively. The higher relative concentration of Ca in GFAGPRA is attributed to the stronger bonding between Ca cations and electronegative GO nanoplatelets, which reduced the leaching of Ca during the F/T process. In contrast, the relative concentration of Al showed an opposite trend. This may be due to the fact that this was relative concentration rather than physical concentration, and Ca was easier to leach out than Al, and thus resulting in an increased relative concentration of Al after much Ca had leached out.

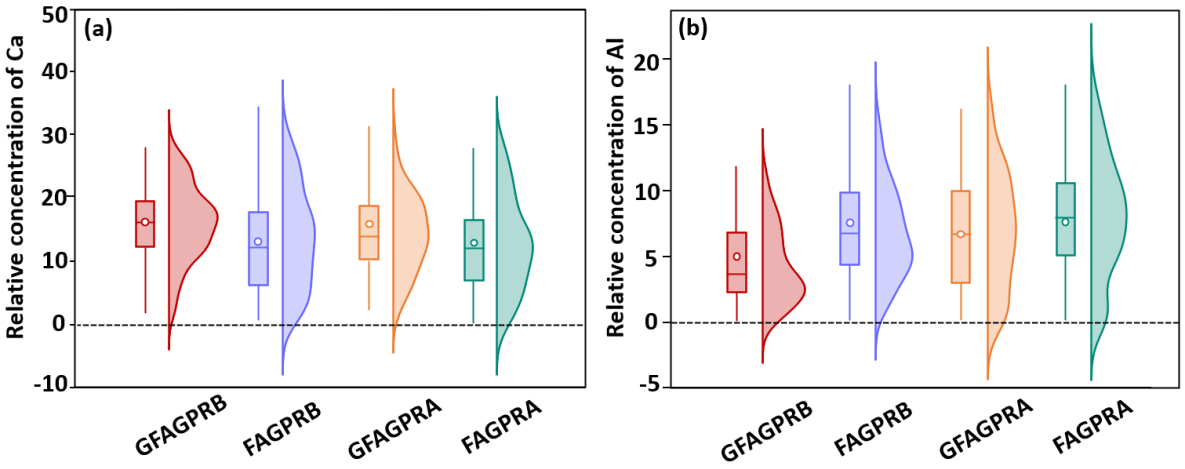

Figure 4.12. The relative concentration along with frequency distribution of (a) Ca and (b) Al from GFAGPRB, FAGPRB, GFAGPRA, and FAGPRA, respectively.

The admixed GO also influenced the key elemental mole ratios and their distribution, both before and after F/T cycles. **Figure 4.13** present the boxplots of Ca/Si and Ca/(Si+Al) mole ratios of the four selected paste specimens, along with their frequency distribution. Ca/Si and Ca/(Si+Al) mole ratios are important indicators for C-S-H and C-A-S-H gels, respectively, and higher Ca/Si or Ca/(Si+Al) ratios indicate higher degrees of polymerization for the hydrates (Davidovits, 1982). As shown in **Figure 4.13a**, the mean value of Ca/Si in GFAGPRB was 2.34, which was similar to the mean Ca/Si value of 2.39 in FAGPRB. However, the median value of Ca/Si in GFAGPRB was 2.07, which is 26.1% higher than the median value of 1.53 in FAGPRB, suggesting that GO facilitated the formation of more hydrates with relatively higher degrees of polymerization. After F/T cycles, the mean value of Ca/Si in both GFAGPRA and FAGPRA decreased in light of the Ca leaching from C-S-H and C-A-S-H gels; however, less Ca leached out in GFAGPRA, suggesting the benefits of negative-charged GO in capturing Ca cations and preventing their leaching, and thus mitigating the degradation of hydrates during the F/T cycles. The mean value of Ca/(Si+Al) in GFAGPRA was about 0.60, higher than the mean value of 0.44 in the FAGPRA, suggesting higher polymerized degree of C-A-S-H in the GFAGPRA. The

result of these two mole ratios helps to explain the higher residual compressive strength of GFAGPRA compared to FAGPRA

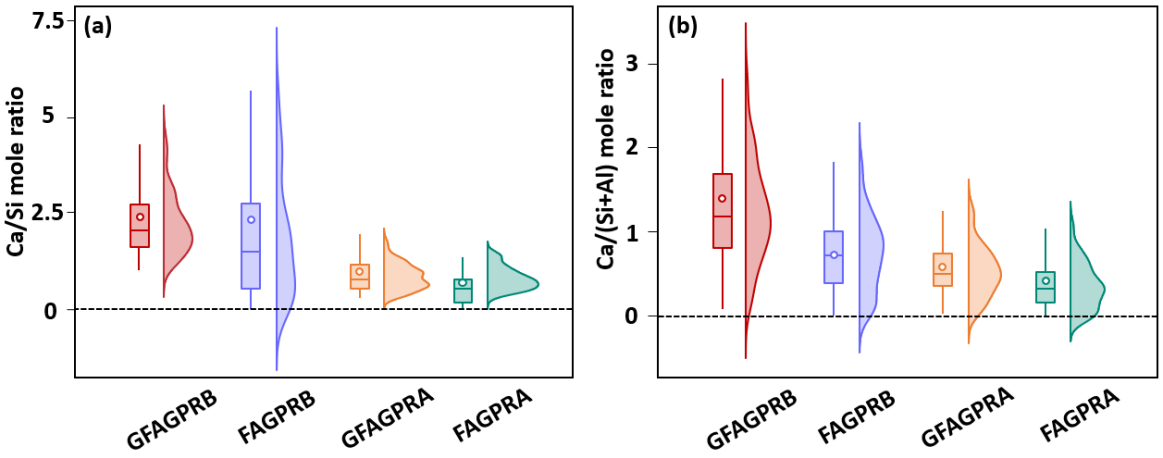

Figure 4.13. The mole ratios along with frequency distribution of (a) Ca/Si and (b) Ca/(Si+Al) from GFAGPRB, FAGPRB, GFAGPRA, and FAGPRA, respectively.

4.4.6 Nuclear Magnetic Resonance Analysis

NMR analysis was conducted to further investigate the influence of GO on the chemical structure and ordering of hydrates (C-S-H and C-A-S-H gels) in GFAGPR before and after F/T cycles, and the results strongly support the EDS and FTIR analysis. **Figure 4.14** illustrates the general rules of 29Si NMR, and the deconvolution analysis of 29Si NMR of selected samples, performed using multi-Gaussian fitting, is provided in **Figure 4.15**. The basic unit of C-S-H and C-A-S-H gels (Si-O tetrahedron) can be categorized into four types based on their location in the chemical structure and ordering (Geng et al., 2024; L. Wang et al., 2021): Q^0 represents the Si-O tetrahedron monomer, Q^1 represents the Si-O tetrahedron located at the end of the Si-based hydrate chains, Q^2 represents the Si-O tetrahedron located in the middle of the Si-based hydrate chains, Q^3 represents the Si-O tetrahedron in the Si-based hydrate network, and Q^4 represents the Si-O tetrahedron in the quartz structure (refer to **Figure 4.14**). The number of adjacent Si-O tetrahedra that are linked to core Si-O tetrahedra increases with the increase of n in Q^n. Moreover, Q^4 is divided into Q^4(mAl) while $m \leqslant 4$, indicating the replaced number of adjacent Si-O by Al-O tetrahedron, which is more predominant in alkali-activated aluminosilicate binder systems. Generally, the higher the n is, the higher the polymerization degree of the binder is, while the lower the hydration reactivity of the raw material is. This trend is consistent with the FTIR results, as discussed in subsection 3.4.

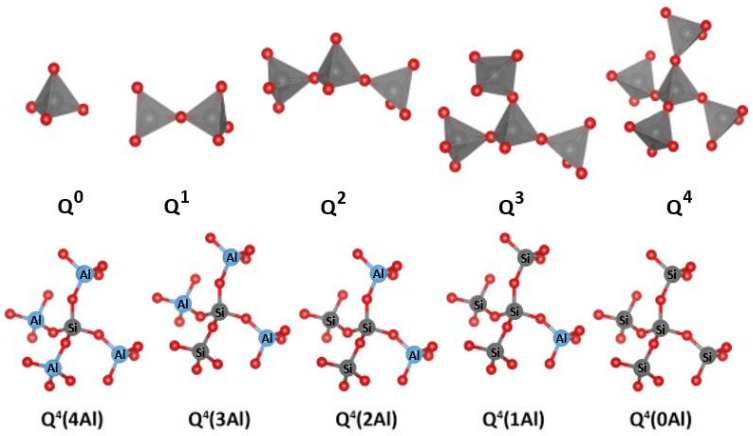

Figure 4.14. Various chemical structures and coordination of Si-O tetrahedron.

Figure 4.15 illustrates the differences in the chemical structures between selected paste specimens, as well as the original fly ash. The ^{29}Si NMR result of fly ash is quite different from paste specimens, indicating a complex alkali-activated pozzolanic reaction involving depolymerization and repolymerization process. During the chemical activation process, the high-polymerized Q^4 in the original fly ash was decomposed into low-polymerized Q^0, Q^1, and Q^2, and then repolymerized into high-polymerized Q^3 and Q^4. The introduction of GO facilitated the generation of higher-polymerized hydrates in GFAGPRB, as compared to FAGPRB. This is evidenced by the decreases in relative area of Q^0 (from 15.36% to 9.23%) and Q^3 (from 18.20% to 0.4%), along with the increases in Q^1 (from 0.3% to 5.49%), Q^2 (from 20.47% to 21.12%), and total Q^4 (from 43.66% to 63.74%) peaks (**Figure 4.15b**). This result is not only supported by FTIR and EDS analysis in this study but also verified by Xu et al. (Xu et al., 2019) who reported a similar result in a GO-modified portland cement system, in which the GO decreased the relative content of Q^0 from 7.9% to 0.2% but increased the Q^1, Q^2, and Q^4 from 53.7% to 55.9%, 36.6% to 40.4%, and 1.8% to 3.5%, respectively. After exposure to F/T cycles, the remaining Q^0, Q^1, and Q^2 in the GFAGPRA paste were about 3.6%, 46.9%, and 34.3% lower than these in FAGPRA; while Q^3 and Q^4 were about 202% and 19.1% higher than these in FAGPRA, respectively, suggesting that GO helped to maintain the chemical structure of FAGPR in aggressive servicing environment. This finding is in accordance with the aforementioned results of residual compressive strength, FTIR, and EDS. Furthermore, GO also modified the coordination of Al-O in Q4(mAl). Contrasting the FAGPRB and GFAGPRB pastes, the introduction of GO increased the Q4(3Al), Q4(2Al), and Q4(1Al) from 4.77% to 38.02%, 5.14% to 10.53%, and 5.22% to 6.64%; however, the relative content of Q4(4Al) in GFAGPRB was much lower than that in FAGPRB (0.17% vs. 20.03%), likely due to the $[Al(OH)_4^-]$ repelling effect of GO, which was revealed in the EDS analysis.

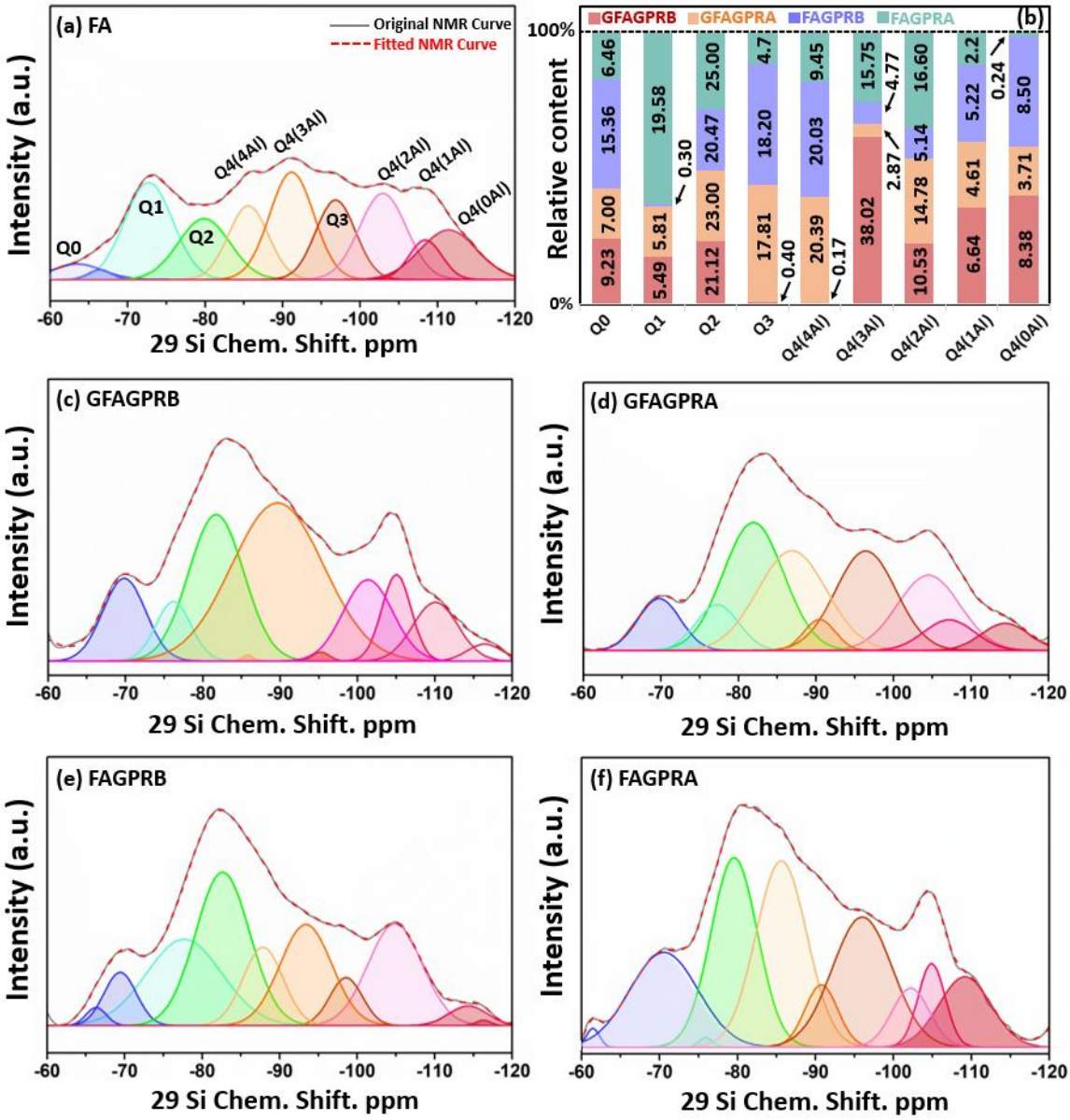

Figure 4.15. 29Si NMR analyses for (a) fly ash, (c) GFAGPRB, (d) GFAGPRA, (e) FAGPRB, and (f) FAGPRA, and (b) summarized the relative area of various peaks for each paste samples.

4.5 Concrete-filled CFRP tube composite

4.5.1 Axial Compressive Tress-Strain Curve

Figure 4.16 presents the axial compressive stress-strain curves for both FAGPR concrete and the FAGPR-filled CFRP tube composite. The concrete specimens used for the comparison are of equal size, measuring 10 cm in diameter and 20 cm in height. Note that the three types of concrete and their corresponding CFRP tube composites exhibit similar trends, with FAGPR concrete serving as a representative example. In the case of unconfined FAGPR concrete, the stress-strain curve initially showed a nearly linear increase, followed by a rapid drop after reaching the peak point (**Figure 4.16a**). This behavior aligns well with

the descriptions found in the previous literature source regarding FAGPR and OPC concretes (Noushini et al., 2016).

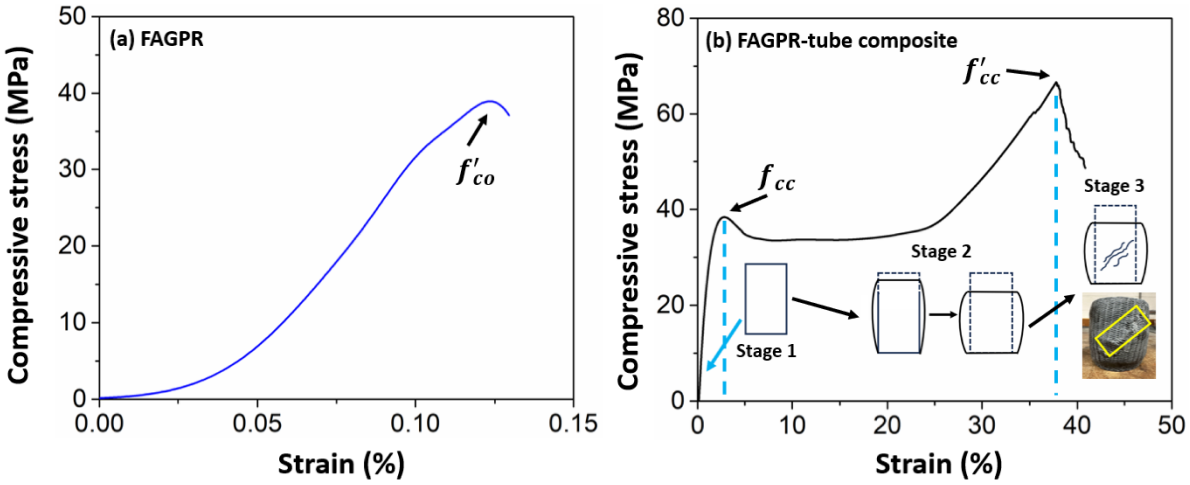

Figure 4.16. The compressive stress-strain behavior of (a) FAGPR concrete and (b) FAGPR concrete-filled CFRP tube composite, respectively.

In contrast, the stress-strain curve for the FAGPR-filled CFRP tube composite demonstrates distinct characteristics. It can be divided into three stages as follows. The first stage features a linear elastic behavior, which resembles the behavior of unconfined FAGPR concrete, with a linear increase leading to the first inflection point. The second stage primarily involves plastic deformation of the FAGPR-filled CFRP tube composite under increasing loading. During this stage, the stress first decreases slightly and then stabilizes in the form of a "crushing plateau" that translates to a great amount of energy absorption. The stress finally increases again in a nearly linear fashion (in the form of densification), eventually reaching the second inflection point. This point is defined as the confined compressive strength ((f'_{cc}), while the corresponding strain is referred to as the defined rupture failure strain ($\varepsilon_{f,rup}$). It was important to note that, unlike the stress, the strain increased significantly, indicating large axial deformation of the CFRP tube under axial loading. The deformation of specimens in the second stage is illustrated in **Figure 4.16b** as well. The third stage (descending stage) commences at the second inflection point, signifying the failure of the specimen. These observations shed light on the mechanical behavior and failure modes of both the FAGPR concrete and the FAGPR-filled CFRP tube composite under axial compression.

The stress-strain behavior of CFRP tube concrete illustrated in **Figure 4.16** suggests that such composites can absorb a great amount of fracture energy and retain a certain level of load-bearing capacity after the initiation of damage. These characteristics of CFRP tube concrete columns could play a significant role in post-event recovery and disaster resiliency of communities, (and mitigate) shortcomings of conventional structural systems under multiple hazards. The primary enhancement mechanism lies in the CFRP tube's fully encasing configuration around the concrete core. This design ensures a more uniform and

effective stress distribution, minimizing the risk of premature failure at localized weak points. Additionally, the CFRP tube provides both axial and lateral confinement, significantly improving resistance to failure under compressive loads. Studies on integrated confinement systems have consistently highlighted the superior performance of such configurations (Li et al., 2016). The progressive failure mechanisms of CFRP tube concrete, as seen in **Figure 4.16b**, can be divided into three stages. Stage 1 represents the elastic behavior of the composite, governed predominantly by the concrete core. Stage 2 marks the interaction between the concrete core and the CFRP tube, where confinement mitigates crack propagation and delays failure. Stage 3 showcases the residual load-bearing capacity of the CFRP tube after the concrete core has reached its peak strength, providing critical resilience against catastrophic collapse.

The post-cracking resilient behavior of CFRP tube concrete sets them from CFRP-wrapped concrete composites. In numerous studies focusing on the latter, only the first peak in the stress-strain curve was documented, and the absence of a second peak was observed. This difference arises from the confinement mechanism: the CFRP wrapping often has weaker connections at joints, resulting in lower structural integrity and ductility compared to the seamless confinement provided by the CFRP tube (Lei et al., 2024, 2021). In summary, the uniform stress distribution, multi-axial confinement, and progressive failure mechanism collectively contribute to the superior performance of CFRP tube concrete. These properties make it a viable option for resilient infrastructure capable of withstanding multiple hazards and ensuring post-event functionality.

4.5.2 Mechanical Modeling

The mechanical testing results, along with the corresponding dimensions (D: outer diameter, H: height, and T: thickness) of the designed cylindrical composite specimens, are outlined in **Table 4.2**. Additionally, the design model specified by ACI 440.2R (**Equation 4.3**) and the function of confined pressure (f_l) exerted by the CFRP tube during loading (**Equations 4.4 and 4.5**) are provided below (Soudki and Alkhrdaji, 2012). The calculated parameters based on these equations are provided in **Table 4.2** as well.

$$f'_{cc} = f'_{co} + \mu_f k_a f_l \tag{4.3}$$

$$f_l = 2f_{f,rup}/D_{i,rup} \tag{4.4}$$

$$f_{f,rup} = E_{frp}\varepsilon_{f,rup}k_\varepsilon T \tag{4.5}$$

Where f'_{cc} is the confined compressive strength, f'_{co} is the compressive strength of core concrete, μ_f is the defined reduction factor, k_a is the shape factor ($k_a = 1$ for circular sections), $f_{f,rup}$ is the ultimate tensile stress of CFRP, E_{frp} is the elastic modulus of CFRP tube (~234 GPa), $\varepsilon_{f,rup}$ is the measured lateral ultimate strain of concrete filled CFRP tube composite, k_ε is the strain efficiency factor ($k_\varepsilon = 0.55$ for design), T is the thickness of CFRP tube, and $D_{i,rup}$ is the inner diameter of CFRP when failure occurs. **Figure 4.17** explains the confined pressure (f_l) and inner diameter $D_{i,rup}$ when failure occurs. To

simplify the calculation and analysis, in this study, we will use the original inner diameter (D_i) instead of considering the influence of the expansion of the inner diameter ($D_{i,rup}$) on the confined compressive strength. By doing so, the effect of the expansion of the inner diameter on the confined compressive strength will not be taken into account.

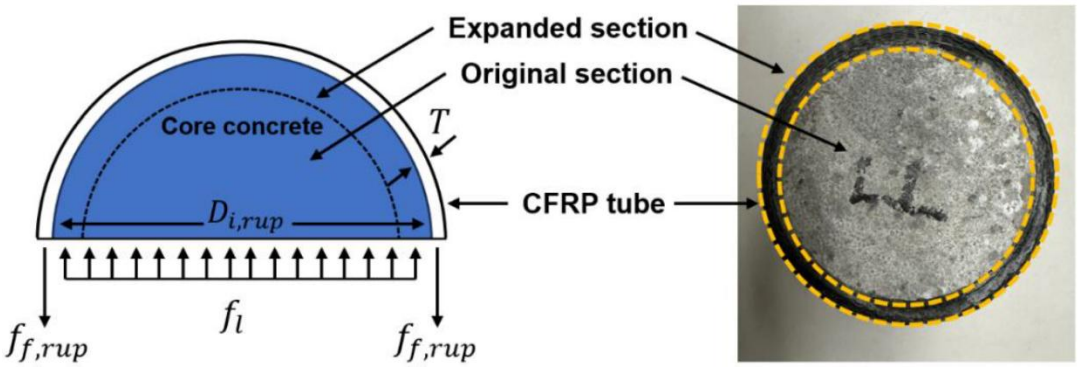

Figure 4.17. Demonstration of confined pressure and inner diameter when failure occurs

Table 4.2. The Mechanical Testing Results of Designed Cylindrical Composite Specimens

Type	f'_{co} (MPa)	f'_{cc} (MPa)	D (cm)	H (cm)	T (cm)	$\varepsilon_{f,rup}$ (%)	f_l (MPa)
OPC-CFRP	57.25	95.01	6.262	12.587	0.231	16.49	1565.77
		88.47	8.253	17.563	0.253	15.33	1362.73
		91.22	10.363	20.257	0.314	17.27	1195.62
FAGPR-CFRP	38.02	69.13	6.255	12.828	0.178	16.90	1237.91
		70.34	7.871	20.028	0.291	17.85	1698.67
		67.10	7.898	18.835	0.203	16.46	1088.97
		64.45	7.955	15.260	0.188	15.13	920.38
		63.20	7.985	15.133	0.212	16.27	1111.88
		67.13	9.090	17.863	0.178	18.75	945.07
		66.38	10.280	25.281	0.327	16.68	1365.71
		64.03	10.333	15.273	0.171	18.44	785.49
		65.34	10.350	15.208	0.175	16.77	729.86
		67.21	10.353	20.303	0.328	15.49	1263.19
		68.97	10.365	15.051	0.314	14.37	1120.54
GFAGPR-CFRP	43.33	75.99	6.281	12.578	0.205	15.48	1300.48
		73.55	6.281	17.577	0.203	15.19	1263.67
		79.14	7.563	20.253	0.264	15.02	1349.55
		75.14	7.901	19.113	0.218	16.66	1183.20
		72.31	7.908	15.143	0.198	18.48	1190.99
		79.21	9.055	18.402	0.314	17.50	1562.02
		75.33	9.075	17.592	0.185	17.60	923.52
		71.03	9.095	21.625	0.188	15.93	847.58
		79.13	10.355	15.045	0.318	16.93	1338.27
		74.21	10.303	20.534	0.207	18.99	982.06
		76.12	10.031	25.258	0.331	17.38	1476.19

Based on the results from **Table 4.2**, the defined reduction factor μ_f can be obtained using the least square method, and three models are proposed as follows:

For OPC concrete-filled CFRP composite:

$$f'_{cc} = 57.25 + 0.0249 f_l \quad (4.6)$$

For FAGPR concrete-filled CFRP composite:

$$f'_{cc} = 38.02 + 0.0246 f_l \quad (4.7)$$

For GFAGPR concrete-filled CFRP composite:

$$f'_{cc} = 43.33 + 0.0259 f_l \quad (4.8)$$

It is important to note that these proposed models are currently at the material level and laboratory scale. As such, they may not be directly applicable for designing a real column. Further research and validation at a larger scale would be necessary before considering their implementation in practical column design. For the sake of sustainability analysis, in this study, we used these models to design structural columns in a very simplified manner.

4.5.3 Sustainability analysis

We assumed an application scenario (e.g., columns in the low-rise buildings to serve in Pullman, WA) before conducting the sustainability analysis for the OPC, FAGPR, GFAGPR concrete-filled CFRP tube composite columns, and the corresponding pure concrete columns. To simplify the design process for these columns employing various materials, the following assumptions have been made. The thickness of the CFRP tube for all columns was uniformly set to 0.5 cm to match larger concrete columns, and a design load of 6,000 kN was assumed for all columns by referring to the research of Zhao et al. (M. Zhao et al., 2021). It is important to mention that the designed compressive strength for all concrete-CFRP tube columns was limited to the corresponding f_{cc} instead of f'_{cc} to avoid the significant deformation (~37% as demonstrated in **Figure 4. 16**) of these columns under the load. Based on these assumptions, the sections of all columns have been designed based on **Equations 4 to 6**, and the results are provided in **Table 4.3**.

Table 4.3. The Section of Designed Columns Based on The Aforementioned Assumptions

Type	Strength* (MPa)	Thickness (cm)	Diameter (cm)	Designed loading capacity (kN)	Actual loading capacity (kN)
OPC-CFRP	58.47	0.5	36.16	6000	6001.5
FAGPR-CFRP	38.89	0.5	44.33	6000	5999.3
GFAGPR-CFRP	44.99	0.5	41.22	6000	6000.7
OPC	57.25	/	36.54	6000	6000.4
FAGPR	38.02	/	44.84	6000	6000.9
GFAGPR	43.33	/	42.00	6000	6000.1

* The strength values of OPC, FAGPR, and GFAGPR-CFRP tube composite were averaged from f_{cc} from **Table 4.2**.

In this study, sustainability was evaluated from both environmental and economic aspects. Environmental sustainability was mainly assessed through the equivalent CO_2 emissions, using data gathered primarily from relevant literature. The unit CO_2 emissions

associated with the production of various materials, represented by their GWP coefficients, are 0.886 kg CO_2/kg for cement (U.S. Cement Industry Carbon Intensities, 2019), 0.00106 kg CO_2/kg for aggregate (Müller et al., 2014), 2.63 kg CO_2/kg for GFRP tube (Li et al., 2013), 0.944 kg CO_2/kg for HRWR (Saade et al., 2020), 1.64 kg CO_2/kg for sodium silicate (City of Winnipeg, 2012), 0.47 kg CO_2/kg for sodium sulfate (City of Winnipeg, 2012), and 0.15 kg CO_2/kg for calcium oxide (City of Winnipeg, 2012), respectively. Fly ash, as a by-product of coal-fired power plants, does not have direct production-related CO_2 emissions, as these emissions are attributed to the power generation process. However, CO_2 emissions associated with transportation (approximately 0.01 kg CO_2/kg of fly ash) and landfilling (approximately 0.04 kg CO_2/kg of fly ash) do exist (U.S. EPA, 2015). In this study, we utilized Class C fly ash, which is widely used in the concrete industry. Since this type of fly ash is typically sourced directly from power plants and not subjected to landfilling, we considered only the transportation-related emissions, assigning a GWP coefficient of 0.01 kg CO_2/kg of fly ash. Regarding graphene oxide (GO), the up-to-date data on its GWP coefficient is not available. However, an estimation could be made based on its energy consumption during production. The estimated GWP coefficient of GO was 125.88 kg CO_2/kg (Serrano-Luján et al., 2019). The GWP coefficients and energy consumption data for producing TIPA and F500 are currently unavailable. Because the dosages of these two components were very small, the GWP coefficient of these two raw materials was simplified to take the average of all chemical reagents (except GO) in this study. **Table 4.** summarizes the GWP coefficients of OPC, FAGPR, and GFAGPR binders used in the research.

Table 4.4. GWP coefficients of OPC, FAGPR, and GFAGPR Binder (kg CO_2/kg)

Binder	Mixture proportion by weight		GWP
OPC	/		***0.886***
FAGPR	Class C FA	100% [86.32%]	0.01
	Na_2SiO_3	6% [5.18%]	1.64
	CaO	3.6% [3.11%]	0.47
	Na_2SO_4	1% [0.86%]	0.15
	TIPA	1.5% [1.29%]	0.75
	F500	3.75% [3.24%]	0.75
	Weighting Sum		***0.136***
GFAGPR	FAGPR	115.85% [99.98%]	0.136
	GO	2% [0.02%]	125.88
	Weighting Sum		***0.158***

Note: The data in [] suggests the relative content of corresponding materials in 1 unit weight of binder.

The economic sustainability was primarily assessed by comparing the costs throughout the entire service life cycle of these columns, including the costs of raw materials, transportation, maintenance, and demolition. The influence of future policies and inflation on the prices is not considered. The price of all raw materials, particularly the chemical reagents, was based on industrial prices rather than quotes from chemical companies supplying for laboratory research. In this work, the price of fly ash was approximately $70.00 per ton, sodium silicate was about $280.00 per ton, sodium sulfate was about $70.00

per ton, calcium oxide was about $160.00 per ton, TIPA was about $2000.00 per ton, F500 was about $1000.00 per ton, coarse aggregate was about $22.00 per ton, fine aggregate was about $50.00 per ton, HRWR was about $300.00 per ton, and the CFRP was about $140.00 per kg. All these price data were obtained from Alibaba, a global industrial wholesale platform. The price of GO was about $180.00 per pound ($396.83 per kg), as provided by CellMark USA, LLC (Shelton, CT), and the price of OPC was about $150.00 per ton based on the data provided by Statista, which references the U.S. Geological Survey, as well as the information from the U.S. Business Environment Profiles (Statista, U.S. cement prices 2010-2023, 2024). Note that these prices may vary across various suppliers. The demolition cost was about $124.20 per cubic meter and the land fill rate was about $0.089 per kg, respectively (Younis et al., 2018). The local hauling cost was about $3.00 per mile, as provided by Heavy Haul and Oversized Company (Ocala, FL). Furthermore, the construction labor salary was approximately $22.29 per hour, based on the mean hourly wage derived from the U.S. Bureau of Labor Statistics. Due to the lack of actual work time data, the construction of all columns was assumed to consume 6 hours and was carried out by four laborers. **Table 4.** summarizes the cost per kg of OPC, FAGPR, and GFAGPR binders used in the research.

Table 4.5. Cost per kg of OPC, FAGPR, and GFAGPR Binder ($/kg)

Binder	Mixture proportion		Cost per kg
OPC	/		***0.15***
FAGPR	Class C FA	100% [86.32%]	0.07
	Na_2SiO_3	6% [5.18%]	0.28
	CaO	3.6% [3.11%]	0.16
	Na_2SO_4	1% [0.86%]	0.07
	TIPA	1.5% [1.29%]	2
	F500	3.75% [3.24%]	1
	Weighting Sum		***0.158***
GFAGPR	FAGPR	115.85% [99.98%]	0.158
	GO	2% [0.02%]	396.83
	Weighting Sum		***0.227***

Note: The data in () suggests the relative content of corresponding materials in 1 unit weight of binder.

To facilitate a fair comparison of the life cycle assessment of OPC, FAGPR, GFAGPR concrete-filled CFRP tube composite columns and the corresponding concrete columns, the following scenarios were proposed:

1. These columns, located in Pullman, WA, were prefabricated by Pre-Mix Inc. (Pullman, WA) and were exposed to the open air. The distance between the construction site and Pre-Mix Inc. was approximately 7.8 miles (12.48 km), while the distance to the local concrete landfill company was about 12.8 miles (20.48 km). The reference (Zhao et al., 2021) provided the GWP coefficients for on-site construction for concrete and CFRP tube were 0.016 and 0.008, respectively. Here, we utilized these coefficients to assess the GWP during the prefabrication process in a factory setting.

2. Considering the historical temperature data in the Pullman area, an average of 7 freeze/thaw cycles were expected annually. Consequently, the projected service life of OPC concrete was estimated to be approximately 30 years (Lei et al., 2021), whereas the estimated service life of (G)FAGPR was about 10 years, as determined from the our working paper regarding the freeze-thaw resistance of (G)FAGPR composite (Li and Shi, 2024).

3. Only uniaxial load was considered. The height of all columns was set to 3 m, and the design load was assumed to be ~6,000 kN and the deformation of these columns under the design load was not considered.

4. The transportation stage in the LCA only focused on the hauling of materials from Pre-Mix Inc. to the construction site in Pullman and the transportation of demolished waste from Pullman to the local landfill company. The GWP coefficient for the hauling was estimated to be 0.6 t*km (Zhao et al., 2021), and the hauling costs was about $3.00 per mile ($1.87 per km), as known from local haul service.

5. Considering the degradation of the columns' performance due to environmental factors such as temperature, moisture, and UV radiation in Pullman, 10% performance loss every 20 years was assumed based on research conducted by Wang and EIGawady (Wang and ElGawady, 2019). Additionally, 10% maintenance activity for CFRP tube was assumed to simply compensate for the performance degradation. The maintenance activities included the material production, transportation, and construction of CFRP (Zhao et al., 2021).

By incorporating these assumptions and considerations into the LCA, we conducted a comprehensive analysis to evaluate the environmental impacts and economic costs of the various concrete filled CFRP tube columns throughout their life span. Based on the mixture proportions of the concrete (Table 3.4), the section sizes (**Table 4.3**), and the height of each column (3m), the amount of materials required for constructing each column was calculated (**Table 4.**). Subsequently, using the GWP coefficients outlined in the previous section, the life-cycle environmental impacts in terms of GWP for each column was estimated. The estimated GWP values of concrete-filled CFRP columns and of pure concrete columns are provided in **Table 4.** and **Table 4.**, respectively. The economic sustainability in terms of life-cycle costs for each column was also assessed, and the estimated cost values of concrete-filled CFRP columns and of pure concrete columns are provided in **Table 4.** and **Table 4.4**, respectively.

Figure 4.18 presents a comparison of the GWP of different columns as a function of service life. The slow increase of GWP observed in the concrete-CFRP tube composite columns is primarily a result of maintenance actions. Conversely, the sharp rise of GWP observed in the concrete-only column is attributed to CO_2 emissions stemming from reconstruction activities. OPC concrete initially exhibits a higher GWP compared to (G)FAGPR concrete columns. Due to the superior freeze/thaw (F/T) durability and a longer

Table 4.6. The weight of Raw Materials Used for Constructing One Column (kg)

Type	Binder	Water	Fine aggregate	Coarse aggregate	HRWR	CFRP
OPC-CFRP	125.065	41.688	187.830	259.395	0.278	0.023
FAGPR-CFRP	206.197	62.187	207.834	306.023	3.142	0.027
GFAGPR-CFRP	181.851	54.844	183.294	269.890	2.771	0.025
OPC	169.782	56.594	254.987	352.140	0.377	/
FAGPR	298.264	89.953	300.631	442.662	4.545	/
GFAGPR	261.712	78.9291	263.790	388.415	3.988	/

service life of approximately 30 years, OPC concrete achieves a lower cumulative GWP over an extended period exceeding 60 years. Specifically, compared with OPC concrete-only columns, FAGPR concrete-only columns exhibit a 19% increase in cumulative GWP, while GFAGPR concrete-only columns show a 12% increase over 100 years of service period. When CFRP tubes are incorporated, the durability of the concrete core becomes less critical, as the tubes mitigate durability concerns. Under these conditions, the lower GWP of the (G)FAGPR binders facilitates a more sustainable solution. Over a 100-year lifespan, OPC-CFRP columns achieve a 28% reduction in cumulative GWP relative to OPC concrete-only columns, while FAGPR-CFRP and GFAGPR-CFRP columns further reduce cumulative GWP by 31% and 34%, respectively. Although GO has a very high GWP, its inclusion in GFAGPR concrete columns reduces cumulative GWP slightly, relative to FAGPR concrete columns. This is primarily due to GO-induced enhancements in compressive strength, which decrease the required column area and reduce the demand for chemical additives with relatively higher GWPs. Additionally, in GFAGPR-CFRP columns, the improved compressive strength of the concrete core reduces the demand for CFRP tube material, which has a high GWP, further contributing to sustainability.

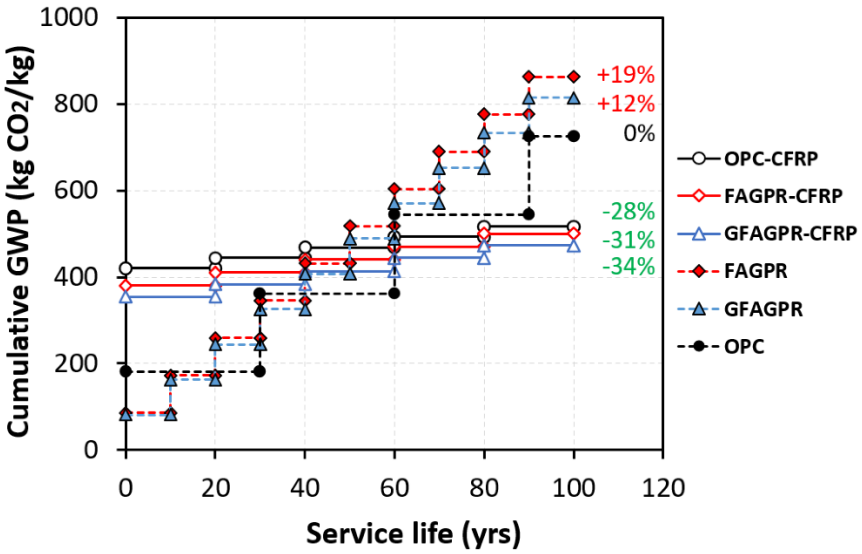

Figure 4.18. The cumulative GWP of different columns as a function of service life

As depicted in **Figure 4.18**, when dealing with temporary structures like columns, piers

for pedestrian bridges, or pile foundations for pavements, concrete-only columns should be considered in light of their reduced CO_2 emissions. Conversely, for components of greater significance with prolonged service life, concrete-CFRP tube composite columns present a more favorable choice. Particularly in specific contexts, such as earthquake-prone regions, the preference should be given to concrete-CFRP tube composite columns due to their exceptional ductile properties and built-in resilience.

Figure 4.19 compares the cumulative costs of various column types as a function of service life. In terms of economic sustainability, an opposing trend to environmental sustainability is evident. Over a 100-year period, OPC-CFRP tube column exhibits a 95% increase in cumulative cost compared to OPC concrete-only columns, while FAGPR-CFRP and GFAGPR-CFRP columns show even higher increases of 135% and 121%, respectively. Despite this, the OPC-CFRP tube column remains more cost-effective than (G)FAGPR-CFRP columns due to the higher compressive strength of OPC concrete, which reduces the required CFRP tube material while maintaining comparable load-bearing capacity. Similarly, GFAGPR-CFRP columns are more economically viable than FAGPR-CFRP columns, as the inclusion of GO enhances compressive strength, thereby decreasing the use of CFRP tubes, which are cost-intensive.

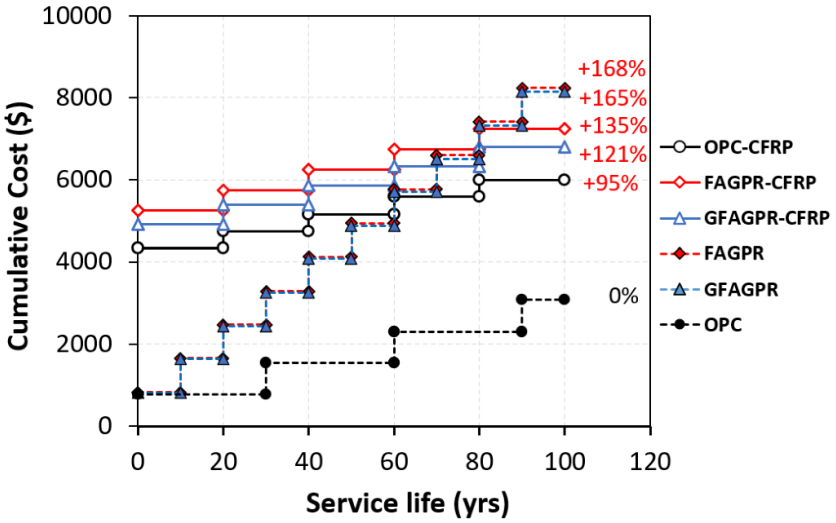

Figure 4.19. The cumulative cost of different columns as a function of service life.

For concrete-only columns, OPC concrete maintains its economic advantage due to its superior F/T durability, which extends service life and reduces reconstruction costs. Compared to OPC concrete-only columns, FAGPR and GFAGPR concrete-only columns exhibit cost increases of 168% and 165%, respectively, because of the re-construction. While the inclusion of GO may initially appear uneconomical due to its high cost, its ability to reduce the use of other raw materials, such as aggregates, chemical reagents, and CFRP tubes, offsets these costs in the long run. Overall, OPC concrete columns are more favorable from an economic perspective due to their cost-efficiency over a long service life. However, achieving a balance between economic and environmental sustainability remains critical for ensuring a holistic approach to sustainable infrastructure development.

Table 4.7. Global Warming Potential (kg CO_2 Equivalent) of Various Concrete-Filled CFRP Tube Columns in 20 Years

Column	LCA-stage	Consumed materials		Amount	Unit	GWP Coeff. (kg/kg)	GWP Result (kg)
Concrete -filled CFRP Tube Columns	Production	Concrete	Binder	166.239 (291.592) [252.056]	kg	0.886 (0.136) [0.158]	147.288 (39.656) [39.825]
			Water	55.413 (87.940) [76.017]	kg	0	0
			Fine aggr.	249.667 (293.906) [254.057]	kg	0.001 (0.001) [0.001]	0.265 (0.312) [0.269]
			Coarse aggr.	344.792 (432.759) [374.083]	kg	0.001 (0.001) [0.001]	0.366 (0.459) [0.397]
			HRWR	0.369 (4.443) [3.841]	kg	0.944 (0.944) [0.944]	0.349 (4.195) [3.626]
		CFRP tube		25.865 (31.635) [29.437]	kg	9.350 (9.350) [9.350]	241.837 (295.785) [275.235]
		Sum		***390.104 (340.406) [319.351]***			
	Transportation (Premix. Inc)	Concrete		10.190 (13.861) [11.982]	t*km	0.600 (0.600) [0.600]	6.114 (8.317) [7.189]
		CFRP tube		0.323 (0.395) [0.367]	t*km	0.600 (0.600) [0.600]	0.194 (0.237) [0.220]
		Sum		***6.307 (18.023) [15.596]***			
	Construction	Concrete		816.480 (1110.640) [960.053]	kg	0.016 (0.016) [0.016]	13.064 (17.770) [15.361]
		CFRP tube		25.865 (31.635) [29.437]	kg	0.008 (0.008) [0.008]	0.207 (0.253) [0.236]
		Sum		***13.271 (18.023) [15.596]***			
	Maintenance	CFRP tube		*Use about 10% material (CFRP) to roughly compensate for the 10% performance loss every 20 yrs.*			
		Sum		***0 (0) [0]***			
	End-of-life (landfill location)	Concrete		16.722 (22.746) [19.662]	t*km	0.600 (0.600) [0.600]	10.033 (13.648) [11.797]
		CFRP tube		0.530 (0.648) [0.603]	t*km	0.600 (0.600) [0.600]	0.318 (0.389) [0.362]
		Sum		***10.351 (14.036) [12.159]***			
Total Sum				***420.032 (381.019) [354.516]***			

Note: (1) The data, (data), and [data] are for OPC, FAGPR, and GFAGPR concrete, respectively.

(2) Maintenance is assumed to be conducted every 20 years for longer service life, it is supposed to emit about 10%*(241.837+0.194+0.207) =24.224 kg CO_2 for OPC-CFRP column, (29.628) kg CO_2 for FAGPR-CFRP column, and [27.569] kg CO_2 for GFAGPR-CFRP column, respectively.

(3) The maintenance-related CO_2 emissions (kg) between 20~40, 40~60, 60~80, and 80~100 year are assumed to be 24.224 (29.628) [27.569], 48.448 (59.256) [55.138], 72.671 (88.883) [82.707], and 96.895 (118.510) [110.276] for OPC, FAGPR, GFAGPR-CFRP columns, respectively.

Table 4.8. Global Warming Potential (kg CO_2) of OPC Column For 30 Years and (G)FAGPR Columns For 10 Years.

Column	LCA-stage	Consumed materials		Amount	Unit	GWP Coeff.	GWP Result
Concrete Columns	Production	Concrete	Binder	169.782 (298.264) [261.712]	kg	0.886 (0.136) [0.158]	150.427 (40.564) [41.350]
			Water	56.594 (89.953) [78.929]	kg	0	0
			Fine aggr.	254.987 (300.631) [263.790]	kg	0.001 (0.001) [0.001]	0.270 (0.319) [0.280]
			Coarse aggr.	352.140 (442.662) [388.415]	kg	0.001 (0.001) [0.001]	0.373 (0.469) [0.412]
			HRWR	0.377 (4.545) [3.988]	kg	0.944 (0.944) [0.944]	0.356 (4.291) [3.765]
		Sum		***151.426 (45.642) [45.807]***			
	Transportation (Premix. Inc)	Concrete		10.407 (14.178) [12.441]	t*km	0.600 (0.600) [0.600]	6.244 (8.507) [7.464]
		Sum		***6.244 (8.507) [7.464]***			
	Construction	Concrete		833.880 (1136.055) [996.834]	kg	0.016 (0.016) [0.016]	13.342 (18.177) [15.949]
		Sum		***13.342 (18.177) [15.949]***			
	End-of-life (landfill location)	Concrete		17.078 (23.266) [20.415]	t*km	0.600 (0.600) [0.600]	10.247 (13.960) [12.249]
		Sum		***10.247 (13.960) [12.249]***			
Total Sum				***181.259 (86.286) [81.469]***			

Note: (1) To simplify the scenario, no maintenance is considered for concrete-only columns, with reconstruction taking place following the demolition.

(2) The cumulative (re)construction-related CO_2 emissions (kg) between 0~30, 30~60, 60~90, and 90~120 years for OPC column are assumed to be 181.259, 362.518, 543.777, and 725.036, respectively.

(3) The cumulative (re)construction-related CO_2 emissions (kg) between 0~10, 10~20, 20~30, 30~40, 40~50, 50~60, 60~70, 70~80, 80~90, and 90~100 years for FAGPR and GFAGPR are assumed to be (86.286)[81.469], (172.572)[162.938], (258.858)[244.407], (345.144)[325.876], (431.430)[407.345], (517.716)[488.814], (604.002)[570.283], (690.288)[651.752], (776.574)[733.221], and (862.860)[814.690], respectively.

Table 4.9. Economic Cost ($) of Various Concrete-Filled CFRP Tube Columns in 20 Years

Column	LCA-stage	Item		Amount	Unit	Cost per unit	Cost
Concrete -filled CFRP Tube Columns	Production	Concrete	Binder	166.239 (291.592) [252.056]	kg	0.150 (0.139) [0.207]	24.936 (40.473) [52.251]
			Water	55.413 (87.940) [76.017]	kg	0	0
			Fine aggr.	249.667 (293.906) [254.057]	kg	0.050 (0.050) [0.050]	12.483 (14.695) [12.703]
			Coarse aggr.	344.792 (432.759) [374.083]	kg	0.022 (0.022) [0.022]	7.585 (9.521) [8.230]
			HRWR	0.369 (4.443) [3.841]	kg	0.300 (0.300) [0.300]	0.111 (1.333) [1.152]
		CFRP tube		25.865 (31.635) [29.437]	kg	140.00 (140.00) [140.00]	3621.088 (4429.867) [4121.160]
		Sum		***3666.203 (4494.889) [4121.160]***			
	Transportation (Premix. Inc)	Prefabricated columns		12.480 (12.480) [12.480]	km	1.870 (1.870) [1.870]	23.338 (23.338) [23.338]
		Sum		***23.338 (23.338) [23.338]***			
	Construction	Labor cost		6.000 (6.000) [6.000]	hour	22.290 (22.290) [22.290]	534.960 (534.960) [534.960]
		Sum		***534.960 (534.960) [534.960]***			
		CFRP tube		*Use about 10% material (CFRP)to roughly compensate for the 10% performance loss.*			
		Sum		***0 (0) [0]***			
	End-of-life (landfill location)	Demolition		0.308 (0.463) [0.400]	m^3	124.20 (124.20) [124.20]	38.241 (57.485) [49.691]
		Transportation		20.480 (20.480) [20.480]	km	1.870 (1.870) [1.870]	38.298 (38.298) [38.298]
		Land fill rate		842.345 (1142.275) [989.490]	kg	0.089 (0.089) [0.089]	74.969 (101.663) [88.065]
		Sum		***151.508 (197.445) [176.053]***			
Total Sum				***4327.008 (5250.631) [4929.847]***			

Note: (1) The data, (data), and [data] are for OPC, FAGPR, and GFAGPR concrete, respectively.

(2) Maintenance is assumed to be conducted every 20 years for longer service life, it is supposed to cost about 10%*(3621.088+23.338+534.960) = $417.939 for OPC-CFRP column, $ (498.716) for FAGPR-CFRP column, and $ [467.946] for GFAGPR-CFRP column, respectively.

(3) The maintenance-related cost ($) between 20~40, 40~60, 60~80, and 80~100 years are assumed to be 417.939 (498.716) [467.946], 835.877 (997.432) [935.891], 1253.816 (1496.149) [1043.837], and 1671.754 (1994.866) [1871.783] for OPC, FAGPR, GFAGPR-CFRP columns, respectively.

Table 4.4. Economic Cost ($) of OPC Column For 30 Years and (G)FAGPR Columns For 10 Years

Column	LCA-stage	Consumed materials		Amount	Unit	Cost per unit	Cost
Concrete Columns	Production	Concrete	Binder	169.782 (298.264) [261.712]	kg	0.150 (0.128) [0.171]	28.294 (41.399) [54.253]
			Water	56.594 (89.953) [78.929]	kg	0	0
			Fine aggr.	254.987 (300.631) [263.790]	kg	0.050 (0.050) [0.050]	12.749 (15.032) [13.190]
			Coarse aggr.	352.140 (442.662) [388.415]	kg	0.022 (0.022) [0.022]	7.747 (9.739) [8.545]
			HRWR	0.377 (4.545) [3.988]	kg	0.300 (0.300) [0.300]	0.113 (1.364) [1.196]
		Sum		***51.192 (75.032) [49.322]***			
	Transportation (Premix. Inc)	Prefabricated columns		12.480 (12.480) [12.480]	km	1.870 (1.870) [1.870]	23.338 (23.338) [23.338]
		Sum		***23.338 (23.338) [23.338]***			
	Construction	Labor cost		6.000 (6.000) [6.000]	hour	22.290 (22.290) [22.290]	534.960 (534.960) [534.960]
		Sum		***534.960 (534.960) [534.960]***			
	End-of-life (landfill location)	Demolition		0.314 (0.473) [0.415]	m^3	124.20 (124.20) [124.20]	43.383 (58.796) [51.595]
		Transportation		20.480 (20.480) [20.480]	km	1.870 (1.870) [1.870]	38.298 (38.298) [38.298]
		Land fill rate		833.880 (1136.055) [996.834]	kg	0.089 (0.089) [0.089]	74.215 (101.109) [88.718]
		Sum		***155.896 (198.203) [178.611]***			
Total Sum				***769.290 (824.033) [814.092]***			

Note: (1) To simplify the scenario, no maintenance is considered for concrete-only columns, with reconstruction taking place following the demolition.

(2) The cumulative (re)construction cost ($) between 0~30, 30~60, 60~90, and 90~120 years for OPC column are assumed to be 769.290, 1538.580, 2307.870, and 3077.160, respectively.

(3) The cumulative (re)construction cost ($) between 0~10, 10~20, 20~30, 30~40, 40~50, 50~60, 60~70, 70~80, 80~90, and 90~100 years for FAGPR and GFAGPR are assumed to be (824.033)[814.092], (1648.066)[1628.184], (2472.099)[2442.276], (3296.132)[3256.368], (4120.165)[4070.460], (4944.198)[4884.552], (5768.231)[5698.644], (6592.264)[6512.736], (7416.297)[7326.828], and (8240.330)[8140.92], respectively.

Chapter 5. Summary and Conclusions

This study systematically explored the development, characterization, and structural application of a graphene oxide (GO)-modified, alkali-activated fly ash-based geopolymer binder and its integration into CFRP tube-confined composite systems. Through a multiscale approach spanning from materials formulation to structural performance evaluation and life cycle sustainability analysis, the following major findings and conclusions are drawn:

1. The incorporation of a small amount of GO (0.02 wt% relative to fly ash) significantly improved the compressive strength, workability, setting behavior, dimensional stability, and water resistance of the geopolymer binder. GO functioned as both a nano-filler and a chemically active agent that enhanced the distribution, polymerization, and stability of C-(A)-S-H gels. These effects were confirmed through a suite of microscopic and spectroscopic tools including SEM, XRD, FTIR, NMR, and TGA.
2. The GO-modified geopolymer exhibited superior resistance to freeze–thaw degradation, retaining over 90% of its compressive strength after 84 cycles, compared to just 67% for the control binder. GO effectively reduced calcium leaching, refined microstructure, and mitigated microcrack propagation, demonstrating its potential for infrastructure applications in cold and wet climates.
3. When used as the core material in CFRP tube-confined composites, the GO-enhanced geopolymer concrete demonstrated exceptional mechanical performance. Confined compressive strength reached up to 79 MPa, with pronounced improvements in ductility, post-peak resilience, and strain capacity. Experimental results closely aligned with theoretical confinement models (ACI 440.2R), and the mechanical synergy between GO-modified core and CFRP shell was validated.
4. The life cycle assessment showed that GFAGPR-CFRP composites can reduce global warming potential (GWP) by more than 30% compared to OPC-CFRP systems while maintaining equivalent load-bearing capacity. Although CFRP incurs higher material cost, the reduced usage enabled by enhanced core strength offsets a portion of this burden, resulting in a well-balanced sustainability-cost-performance profile over a 100-year service life.

This study provided several important experimental insights regarding the development and evaluation of GO-modified geopolymer binders and geopolymer-filled CFRP tube systems. First, the effectiveness of graphene oxide incorporation was found to be sensitive to dispersion quality and mixing procedures. Minor variations in GO dispersion, alkaline activator preparation, or mixing sequence may influence gel formation and early-age mechanical performance, highlighting the need for standardized and repeatable processing protocols for scale-up.

Second, the freeze–thaw durability assessment was conducted using accelerated laboratory testing in accordance with ASTM C666, which provides valuable comparative performance data but cannot fully capture the combined effects of sustained mechanical loading, moisture transport, and environmental variability encountered under long-term field exposure. As a result, laboratory-observed durability improvements may differ in magnitude when translated to in-service conditions.

Third, the fabrication and testing of geopolymer-filled CFRP tube specimens were performed at the laboratory scale, where geometric tolerances, confinement efficiency, and boundary conditions are more tightly controlled than in full-scale structural applications. Variability associated with field construction practices and large-scale manufacturing may affect composite performance and should be addressed through pilot-scale testing and validation.

Overall, these lessons emphasize that while GO-engineered geopolymer binders and geopolymer-filled CFRP tube systems demonstrate strong potential for structural and durability-critical applications, further refinement of processing consistency, scaling methodology, and field-level validation is necessary to ensure reliable and reproducible performance in practical infrastructure implementation. Future research is recommended in the following areas:

1. Long-Term Durability Studies: Investigate resistance to other environmental stressors such as sulfate attack, chloride penetration, and high-temperature exposure.
2. Field-Scale Validation: Implement pilot-scale field tests to evaluate constructability, in-situ performance, and material aging under real environmental conditions.
3. Multi-Hazard Resilience Modeling: Extend structural performance assessment to include seismic, impact, and fire scenarios.
4. Smart Monitoring Integration: Explore the use of self-sensing capabilities enabled by GO or additional nanomaterials for real-time structural health monitoring.
5. Standardization and Scaling: Develop material design guidelines and prequalification protocols to facilitate code integration and commercialization pathways.

Chapter 6. Technology Transfer and Implementation

The outcomes of this study demonstrate strong potential for transitioning GO-engineered geopolymer and geopolymer-filled CFRP tube systems from laboratory-scale research to practical infrastructure applications. The combined improvements in mechanical performance, durability, and environmental sustainability provide a clear foundation for technology transfer and implementation in transportation and structural engineering contexts.

6.1 Potential Applications

Based on the experimentally demonstrated strength enhancement, freeze–thaw durability, and confinement performance, the proposed materials are well suited for a range of structural and transportation infrastructure applications. Potential applications include concrete-filled CFRP tubes for bridge columns, piles, and piers; structural members in cold-region infrastructure exposed to cyclic freeze–thaw conditions; and precast structural elements where high strength, durability, and dimensional stability are required. The improved freeze–thaw resistance and reduced moisture ingress of the GO-modified geopolymer further support its applicability in durability-critical environments.

6.2 Prospective Users and Stakeholders

Prospective users of this technology include state and local Departments of Transportation (DOTs), particularly DOT materials laboratories responsible for evaluating and qualifying innovative cementitious and composite systems. Precast concrete manufacturers and structural composite producers also represent key stakeholders, as the geopolymer binder and geopolymer-filled CFRP tube systems can be integrated into controlled manufacturing environments with minimal changes to existing fabrication processes. Additional stakeholders include bridge engineers, infrastructure owners, and contractors seeking durable, low-carbon alternatives to conventional OPC-based structural systems.

6.3 Expected Cost and Life-Cycle Benefits

Although detailed cost analysis was beyond the scope of this study, the use of clinker-free, fly ash-based geopolymer binders offers a pathway to reduce reliance on ordinary Portland cement and associated greenhouse gas emissions. Life cycle assessment results demonstrated that GFAGPR-filled CFRP tube systems can reduce global warming potential by more than 30% compared to conventional OPC-based CFRP composites over a 100-year service life.

From a life-cycle perspective, the enhanced compressive strength and durability of the GO-modified geopolymer core enable reduced CFRP material demand, improved structural efficiency, and extended service life. These factors are expected to decrease maintenance frequency and long-term rehabilitation needs, thereby offsetting higher initial material costs associated with CFRP and yielding a balanced sustainability–cost–performance profile for long-term infrastructure applications.

References

Abdalla, J.A., Thomas, B.S., Hawileh, R.A., Yang, J., Jindal, B.B., Ariyachandra, E., 2022. Influence of nano-TiO_2, nano-Fe_2O_3, nanoclay and nano-$CaCO_3$ on the properties of cement/geopolymer concrete. Cleaner Materials 4, 100061. https://doi.org/10.1016/j.clema.2022.100061

Ahmari, S., Zhang, L., 2013. Utilization of cement kiln dust (CKD) to enhance mine tailings-based geopolymer bricks. Construction and Building Materials, Special Section on Recycling Wastes for Use as Construction Materials 40, 1002–1011. https://doi.org/10.1016/j.conbuildmat.2012.11.069

Alrshoudi, F., Abbas, H., Abadel, A., Albidah, A., Altheeb, A., Al-Salloum, Y., 2021. Compression behavior and modeling of FRP-confined high strength geopolymer concrete. Construction and Building Materials 283, 122759. https://doi.org/10.1016/j.conbuildmat.2021.122759

Andrew, R.M., 2018. Global CO_2 emissions from cement production. Earth System Science Data 10, 195–217. https://doi.org/10.5194/essd-10-195-2018

Davidovits, J., 1982. Mineral polymers and methods of making them. US4349386A.

City of Winnipeg., 2012. Emission Factors in Kg CO_2-Equivalent per Unit.

U.S. EPA., 2015. Fly ash-EPA Waste Reduction Model.

Geng, Z., Tang, S., Wang, Y., A., H., He, Z., Wu, K., Wang, L., 2024. Stress relaxation properties of calcium silicate hydrate: a molecular dynamics study. J. Zhejiang Univ. Sci. A 25, 97–115. https://doi.org/10.1631/jzus.A2300476

Gong, J., Qian, Y., Xu, Z., Chen, C., Jin, Y., Zhang, J., Li, Z., Shi, X., 2024. Effect of graphene oxide on the properties of ternary limestone clay cement paste. Nanotechnology Reviews 13, 20230222. https://doi.org/10.1515/ntrev-2023-0222

Gong, J., Yu, L., Li, Z., Shi, X., 2022. Mechanical activation improves reactivity and reduces leaching of municipal solid waste incineration (MSWI) bottom ash in cement hydration system. Journal of Cleaner Production 363, 132533. https://doi.org/10.1016/j.jclepro.2022.132533

Goonewardena, J., Ghabraie, K., Subhani, M., 2020. Flexural Performance of FRP-Reinforced Geopolymer Concrete Beam. Journal of Composites Science 4, 187. https://doi.org/10.3390/jcs4040187

Han, Q., Zhang, P., Wu, J., Jing, Y., Zhang, D., Zhang, T., 2022. Comprehensive review of the properties of fly ash-based geopolymer with additive of nano-SiO_2. Nanotechnology Reviews 11, 1478–1498. https://doi.org/10.1515/ntrev-2022-0092

Hassan, A., Arif, M., Shariq, M., 2020. A review of properties and behavior of reinforced geopolymer concrete structural elements- A clean technology option for sustainable development. Journal of Cleaner Production 245, 118762. https://doi.org/10.1016/j.jclepro.2019.118762

He, Y., Chen, Q., Yang, S., Lu, C., Feng, M., Jiang, Y., Cao, G., Zhang, J., Liu, C., 2018. Micro-crack behavior of carbon fiber reinforced Fe3O4/graphene oxide modified epoxy composites for cryogenic application. Composites Part A: Applied Science and Manufacturing 108, 12–22. https://doi.org/10.1016/j.compositesa.2018.02.014

Huang, T., Sun, Z., 2021. Advances in multifunctional graphene-geopolymer composites. Construction and Building Materials 272, 121619. https://doi.org/10.1016/j.conbuildmat.2020.121619

Khater, H.M., El-Sabbagh, B.A., Fanny, M., Ezzat, M., Lottfy, M., Nagar, A.M.E., 2013. Effect of Nano-Clay on Alkali Activated Water-Cooled Slag Geopolymer. Current Journal of Applied Science and Technology 764–776. https://doi.org/10.9734/BJAST/2013/2690

Kumar, S., Mucsi, G., Kristály, F., Pekker, P., 2017. Mechanical activation of fly ash and its influence on micro and nano-structural behaviour of resulting geopolymers. Advanced Powder Technology 28, 805–813. https://doi.org/10.1016/j.apt.2016.11.027

Lahoti, M., Tan, K.H., Yang, E.-H., 2019. A critical review of geopolymer properties for structural fire-resistance applications. Construction and Building Materials 221, 514–526. https://doi.org/10.1016/j.conbuildmat.2019.06.076

Lee, N.K., Jang, J.G., Lee, H.K., 2014. Shrinkage characteristics of alkali-activated fly ash/slag paste and mortar at early ages. Cement and Concrete Composites 53, 239–248. https://doi.org/10.1016/j.cemconcomp.2014.07.007

Lei, Z., Li, Z., Zhang, X., Shi, X., 2021. Durability of CFRP-wrapped concrete in cold regions: A laboratory evaluation of montmorillonite nanoclay-modified siloxane epoxy adhesive. Construction and Building Materials 290, 123253. https://doi.org/10.1016/j.conbuildmat.2021.123253

Lei, Z., Xiao, T., Yang, C., Li, Z., Shi, X., 2024. Improving the performance of CFRP-reinforced concrete cylinders in sulfate-laden environment through nanoclay modification of epoxy resin. Construction and Building Materials 436, 136860.

Li, Y.-F., Yu, C.-C., Chen, S.-Y., Sainey, B., 2013. The Carbon Footprint Calculation of the GFRP Pedestrian Bridge at Tai-Jiang National Park. International Review for Spatial Planning and Sustainable Development 1, 13–28. https://doi.org/10.14246/irspsd.1.4_13

Li, Y.L., Zhao, X.L., Raman Singh, R.K., Al-Saadi, S., 2016. Tests on seawater and sea sand concrete-filled CFRP, BFRP and stainless steel tubular stub columns. Thin-Walled Structures 108, 163–184. https://doi.org/10.1016/j.tws.2016.08.016

Li, Z., Fei, M.-E., Huyan, C., Shi, X., 2021. Nano-engineered, Fly Ash-Based Geopolymer Composites: An Overview. Resources, Conservation and Recycling 168, 105334. https://doi.org/10.1016/j.resconrec.2020.105334

Li, Z., Shi, X., 2025. Influence of graphene oxide on resistance of a fly ash-based geopolymer paste to cyclic freeze-thaw damage and post-damage carbonation. Cement and Concrete Composites 160, 106023. https://doi.org/10.1016/j.cemconcomp.2025.106023

Li, Z., Shi, X., 2024. Freeze-Thaw Resistance of Graphene Oxide-Engineered Fly Ash-Based Geopolymer Paste. working paper.

Li, Z., Shi, X., 2022. Effects of Nanomaterials on Engineering Performance of a Potassium Methyl Siliconate–Based Sealer for Cementitious Composite. Journal of Materials in Civil Engineering 34, 04022006. https://doi.org/10.1061/(ASCE)MT.1943-5533.0004148

Li, Z., Shi, X., 2020. Graphene oxide modified, clinker-free cementitious paste with principally alkali-activated fly ash. Fuel 269, 117418. https://doi.org/10.1016/j.fuel.2020.117418

Li, Z., Xu, G., Shi, X., 2021. Reactivity of coal fly ash used in cementitious binder systems: A state-of-the-art overview. Fuel 301, 121031. https://doi.org/10.1016/j.fuel.2021.121031

Li, Z., Zhang, Z., Fei, M., Shi, X., 2022. Upcycling waste mask PP microfibers in portland cement paste: Surface treatment by graphene oxide. Materials Letters 318, 132238. https://doi.org/10.1016/j.matlet.2022.132238

Liu, C., Huang, X., Wu, Y.-Y., Deng, X., Liu, J., Zheng, Z., Hui, D., 2020. Review on the research progress of cement-based and geopolymer materials modified by graphene and graphene oxide. Nanotechnology Reviews 9, 155–169. https://doi.org/10.1515/ntrev-2020-0014

Lu, D., Shi, X., Zhong, J., 2022. Nano-engineering the interfacial transition zone in cement composites with graphene oxide. Construction and Building Materials 356, 129284. https://doi.org/10.1016/j.conbuildmat.2022.129284

Lu, Z., Li, X., Hanif, A., Chen, B., Parthasarathy, P., Yu, J., Li, Z., 2017. Early-age interaction mechanism between the graphene oxide and cement hydrates. Construction and Building Materials 152, 232–239. https://doi.org/10.1016/j.conbuildmat.2017.06.176

Matos, A.M., Sousa-Coutinho, J., 2012. Durability of mortar using waste glass powder as cement replacement. Construction and Building Materials 36, 205–215. https://doi.org/10.1016/j.conbuildmat.2012.04.027

Min, Y., Wu, J., Li, B., Zhang, M., Zhang, J., 2022. Experimental study of freeze–thaw resistance of a one-part geopolymer paste. Case Studies in Construction Materials 17, e01269. https://doi.org/10.1016/j.cscm.2022.e01269

Mohammed, A., Al-Saadi, N.T.K., Al-Mahaidi, R., 2017. Utilization of Graphene Oxide to Synthesize High-Strength Cement-Based Adhesive. Journal of Materials in Civil Engineering 29, 04016258. https://doi.org/10.1061/(ASCE)MT.1943-5533.0001705

Mohammed, A., Sanjayan, J.G., Duan, W.H., Nazari, A., 2015. Incorporating graphene oxide in cement composites: A study of transport properties. Construction and Building Materials 84, 341–347. https://doi.org/10.1016/j.conbuildmat.2015.01.083

Müller, H.S., Breiner, R., Moffatt, J.S., Haist, M., 2014. Design and Properties of Sustainable Concrete. Procedia Engineering, The 2nd International Conference on Sustainable Civil Engineering Structures and Construction Materials 95, 290–304. https://doi.org/10.1016/j.proeng.2014.12.189

Noushini, A., Aslani, F., Castel, A., Gilbert, R.I., Uy, B., Foster, S., 2016. Compressive stress-strain model for low-calcium fly ash-based geopolymer and heat-cured Portland cement concrete. Cement and Concrete Composites 73, 136–146.

https://doi.org/10.1016/j.cemconcomp.2016.07.004

Saade, M.R.M., Passer, A., Mittermayr, F., 2020. (Sprayed) concrete production in life cycle assessments: a systematic literature review. Int J Life Cycle Assess 25, 188–207. https://doi.org/10.1007/s11367-019-01676-w

Salas, D.A., Ramirez, A.D., Ulloa, N., Baykara, H., Boero, A.J., 2018. Life cycle assessment of geopolymer concrete. Construction and Building Materials 190, 170–177. https://doi.org/10.1016/j.conbuildmat.2018.09.123

Schwarz, N., Neithalath, N., 2008. Influence of a fine glass powder on cement hydration: Comparison to fly ash and modeling the degree of hydration. Cement and Concrete Research 38, 429–436. https://doi.org/10.1016/j.cemconres.2007.12.001

Serrano-Luján, L., Víctor-Román, S., Toledo, C., Sanahuja-Parejo, O., Mansour, A.E., Abad, J., Amassian, A., Benito, A.M., Maser, W.K., Urbina, A., 2019. Environmental impact of the production of graphene oxide and reduced graphene oxide. SN Appl. Sci. 1, 179. https://doi.org/10.1007/s42452-019-0193-1

Shahrajabian, F., Behfarnia, K., 2018. The effects of nano particles on freeze and thaw resistance of alkali-activated slag concrete. Construction and Building Materials 176, 172–178. https://doi.org/10.1016/j.conbuildmat.2018.05.033

Shamsol, A. 'lia S., Apandi, N.M., Zailani, W.W.A., Izwan, K.N.K., Zakaria, M., Zulkarnain, N.N., 2024. Graphene oxide as carbon-based materials: A review of geopolymer with addition of graphene oxide towards sustainable construction materials. Construction and Building Materials 411, 134410. https://doi.org/10.1016/j.conbuildmat.2023.134410

Singh, B., Ishwarya, G., Gupta, M., Bhattacharyya, S.K., 2015. Geopolymer concrete: A review of some recent developments. Construction and Building Materials 85, 78–90. https://doi.org/10.1016/j.conbuildmat.2015.03.036

Soudki, K., Alkhrdaji, T., 2012. Guide for the Design and Construction of Externally Bonded FRP Systems for Strengthening Concrete Structures (ACI 440.2R-02) 1–8. https://doi.org/10.1061/40753(171)159

Su, Z., Hou, W., Sun, Z., 2020. Recent advances in carbon nanotube-geopolymer composite. Construction and Building Materials 252, 118940. https://doi.org/10.1016/j.conbuildmat.2020.118940

Sumesh, M., Alengaram, U.J., Jumaat, M.Z., Mo, K.H., Alnahhal, M.F., 2017. Incorporation of nano-materials in cement composite and geopolymer based paste and mortar – A review. Construction and Building Materials 148, 62–84. https://doi.org/10.1016/j.conbuildmat.2017.04.206

Tang, Z.Q., de Souza, F.B., Sagoe-Crentsil, K., Duan, W., 2024. Enhancing geopolymer performance with silane-functionalized graphene oxide: Efflorescence reduction, pore refinement, and improved high-temperature properties. Construction and Building Materials 440, 137420. https://doi.org/10.1016/j.conbuildmat.2024.137420

Tang, Z.Q., Sui, H., de Souza, F.B., Sagoe-Crentsil, K., Duan, W., 2023. Silane-modified graphene oxide in geopolymer: Reaction kinetics, microstructure, and mechanical

performance. Cement and Concrete Composites 139, 104997. https://doi.org/10.1016/j.cemconcomp.2023.104997

Tone, T., Koga, N., 2021. Thermally Induced Aragonite–Calcite Transformation in Freshwater Pearl: A Mutual Relation with the Thermal Dehydration of Included Water. ACS Omega 6, 13904–13914. https://doi.org/10.1021/acsomega.1c01683

U.S. EPA., 2019. U.S. Cement Industry Carbon Intensities.

Statista., 2024. U.S. cement prices 2010-2023. Statista. URL https://www.statista.com/statistics/219339/us-prices-of-cement/ (accessed 12.22.24).

Wang, K., Zhang, P., Guo, J., Gao, Z., 2021. Single and synergistic enhancement on durability of geopolymer mortar by polyvinyl alcohol fiber and nano-SiO2. Journal of Materials Research and Technology 15, 1801–1814. https://doi.org/10.1016/j.jmrt.2021.09.036

Wang, L., Jin, M., Zhou, S., Tang, S., Lu, X., 2021. Investigation of microstructure of C-S-H and micro-mechanics of cement pastes under NH4NO3 dissolution by 29Si MAS NMR and microhardness. Measurement 185, 110019. https://doi.org/10.1016/j.measurement.2021.110019

Wang, Q., Wang, D., Zhuang, S., 2017. The soundness of steel slag with different free CaO and MgO contents. Construction and Building Materials 151, 138–146. https://doi.org/10.1016/j.conbuildmat.2017.06.077

Wang, S., ElGawady, M.A., 2019. Effects of hybrid water Immersion, environmental exposures, and axial load on the mechanical properties of concrete filled epoxy-based glass fiber reinforced polymer tubes. Construction and Building Materials 194, 311–321. https://doi.org/10.1016/j.conbuildmat.2018.10.232

Williams, P.J., Biernacki, J.J., Walker, L.R., Meyer, H.M., Rawn, C.J., Bai, J., 2002. Microanalysis of alkali-activated fly ash–CH pastes. Cement and Concrete Research 32, 963–972. https://doi.org/10.1016/S0008-8846(02)00734-2

Winnefeld, F., Leemann, A., Lucuk, M., Svoboda, P., Neuroth, M., 2010. Assessment of phase formation in alkali activated low and high calcium fly ashes in building materials. Construction and Building Materials 24, 1086–1093. https://doi.org/10.1016/j.conbuildmat.2009.11.007

Xie, Z., Xi, Y., 2001. Hardening mechanisms of an alkaline-activated class F fly ash. Cement and Concrete Research 31, 1245–1249. https://doi.org/10.1016/S0008-8846(01)00571-3

Xu, G., Du, S., He, J., Shi, X., 2019. The role of admixed graphene oxide in a cement hydration system. Carbon 148, 141–150. https://doi.org/10.1016/j.carbon.2019.03.072

Xu, G., Shi, X., 2020. Fly Ash Geopolymer Pervious Concrete. Concrete International 42, 37–41.

Xu, G., Zhong, J., Shi, X., 2018. Influence of graphene oxide in a chemically activated fly ash. Fuel 226, 644–657. https://doi.org/10.1016/j.fuel.2018.04.033

Younis, A., Ebead, U., Judd, S., 2018. Life cycle cost analysis of structural concrete using seawater, recycled concrete aggregate, and GFRP reinforcement. Construction and Building Materials 175, 152–160. https://doi.org/10.1016/j.conbuildmat.2018.04.183

Zhao, J., Tong, L., Li, B., Chen, T., Wang, C., Yang, G., Zheng, Y., 2021. Eco-friendly geopolymer materials: A review of performance improvement, potential application and sustainability assessment. Journal of Cleaner Production 307, 127085. https://doi.org/10.1016/j.jclepro.2021.127085

Zhao, M., Dong, Y., Guo, H., 2021. Comparative life cycle assessment of composite structures incorporating uncertainty and global sensitivity analysis. Engineering Structures 242, 112394. https://doi.org/10.1016/j.engstruct.2021.112394

Zinkaah, O.H., Alridha, Z., Alhawat, M., 2022. Numerical and theoretical analysis of FRP reinforced geopolymer concrete beams. Case Studies in Construction Materials 16, e01052. https://doi.org/10.1016/j.cscm.2022.e01052